

SCATTERED EMISSION FROM $Z \sim 1$ GALACTIC OUTFLOWSCRYSTAL L. MARTIN¹ ALICE E. SHAPLEY^{2,3} ALISON L. COIL^{4,5} KATHERINE A. KORNEI² NORMAN MURRAY⁶ ANNA PANCOAST¹*Draft version February 25, 2019*

ABSTRACT

Mapping Mg II resonance emission scattered by galactic winds offers a means to determine the spatial extent and density of the warm outflow. Using Keck/LRIS spectroscopy, we have resolved scattered Mg II emission to the east of 32016857, a star-forming galaxy at $z = 0.9392$ with an outflow. The Mg II emission from this galaxy exhibits a P-Cygni profile, extends further than both the continuum and [O II] emission along the eastern side of the slit, and has a constant Doppler shift along the slit which does not follow the velocity gradient of the nebular [O II] emission. Using the Sobolev approximation, we derive the density of Mg^+ ions at a radius of 12 - 18 kpc in the outflow. We model the ionization correction and find that much of the outflowing Mg is in Mg^{++} . We estimate that the total mass flux could be as large as $330 - 500 \text{ M}_{\odot} \text{ yr}^{-1}$, with the largest uncertainties coming from the depletion of Mg onto grains and the clumpiness of the warm outflow. We show that confining the warm clouds with a hot wind reduces the estimated mass flux of the warm outflow and indicates a mass-loading factor near unity in the warm phase alone. Based on the high blue luminosities that distinguish 32016857 and TKRS 4389, described by Rubin et al. (2011), from other galaxies with P-Cygni emission, we suggest that, as sensitivity to diffuse emission improves, scattering halos may prove to be a generic property of star-forming galaxies at intermediate redshifts.

Subject headings:

1. INTRODUCTION

In the baryon-driven picture of galaxy evolution, gas accretion onto galaxies, gas consumption by star formation, and gas ejection by galactic winds shape the properties of galaxies. The only simple aspect of this baryon cycle may be the rate of gas infall into galactic halos, which may follow the mean growth rate of the dark matter. How much of the inflow can cool and fuel star formation, versus being shock heated to the halo virial temperature, remains a largely theoretical debate (Kereš et al. 2005; Dekel & Birnboim 2006; Kereš et al. 2009; Dekel et al. 2009; Bouché et al. 2010; van de Voort et al. 2011; Davé et al. 2012). In practice, it has generally been more straightforward to detect outflowing gas than inflowing gas.

Over a broad redshift range, spectroscopic surveys have empirically described the galaxy population hosting outflows using blueshifted, resonance absorption lines, where the sign of the Doppler shift (relative to the galactic barycenter) unambiguously identifies outflowing gas on the near side of a galaxy. (Shapley et al. 2003; Martin 2005; Tremonti et al. 2007; Sato et al. 2009; Weiner et al. 2009; Chen et al. 2010; Steidel et al. 2010; Heckman et al. 2011; Coil et al. 2011; Erb et al. 2012; Martin et al. 2012, Rubin et al. , in prep). These data provide an accurate picture of which galaxies host outflows, e.g.,

namely those with large concentrations of massive stars (Heckman 2003; Kornei et al. 2012; Law et al. 2012) consistent with theoretical arguments requiring massive star clusters to generate outflows (Murray et al. 2011).

The properties of these outflows, in contrast to their demographics, remain poorly constrained. The outflowing mass flux, for example, is central to galaxy evolution models; yet theoretical models that fit the empirically determined mass function and mass – metallicity relation for galaxies require a mass-loss rate of order the star formation rate (SFR) at mass scales comparable to the Milky Way (Davé et al. 2012; Shen et al. 2012; Creasey et al. 2013; Hopkins et al. 2013; Puchwein & Springel 2013). The location, maximum velocity, and total column density of the warm outflowing gas are not well-constrained by observations of optical and ultraviolet resonance lines in galaxy spectra. The absorbing clouds may lie anywhere along the sightline to the galaxy, and the decline in gas covering fraction with increasing blueshift makes it challenging to detect the highest velocity gas (Martin & Bouché 2009). The hotter wind fluid, which entrains this warm, low-ionization gas, largely eludes direct detection at intermediate redshifts (Tripp et al. 2011).

Two complementary strategies have emerged recently for measuring the spatial extent of low-ionization outflowing gas. First, at large radii, outflows can be mapped with sightlines to background quasars or galaxies. Halo absorption from outflows may be distinguished from gas accretion by its location in bipolar flows which emerge roughly perpendicular to the galactic disk (Bordoloi et al. 2011; Bouché et al. 2012; Kacprzak et al. 2012). Second, although the emission measure of low density gas typically makes halo gas undetectable by direct imaging, photons scattered by halo gas can be directly imaged (Steidel et al. 2011; Rubin et al. 2011; Prochaska et al.

¹ Department of Physics, University of California, Santa Barbara, CA, 93106, cmartin@physics.ucsb.edu

² Department of Physics and Astronomy, University of California, Los Angeles, CA, 90025

³ Packard Fellow

⁴ Center for Astrophysics and Space Sciences, Department of Physics, University of California, San Diego, CA 92093

⁵ Alfred P. Sloan Fellow

⁶ Canadian Institute for Theoretical Astrophysics, 60 St. George Street, University of Toronto, Toronto, ON M5S 3H8, Canada

2011). Combining the information contained in galaxy absorption spectra, resonance emission maps, and sightlines probing galaxy halos should greatly improve the accuracy of the estimated mass-loss rates in outflows.

The most familiar example of resonance scattering involves the Ly α photons produced in H II regions, which are scattered in our direction by interstellar and circumgalactic gas. P-Cygni Ly α line profiles provide direct kinematic evidence for scattering by outflowing gas. In the simplest model, the redshifted emission component is scattered off the back side of an expanding shell while the near side imprints blueshifted, resonance absorption (Pettini et al. 2002; Verhamme et al. 2008). Since spectra of the bluer, less-obscured high-redshift galaxies (Kornei et al. 2010) show these P-Cygni line profiles more frequently than do spectra of more obscured galaxies, the detection of diffuse Ly α emission in stacks of all types of high-redshift, star-forming galaxies was remarkable (Steidel et al. 2011). These halos are apparently common, extend beyond the UV-continuum emission, and indicate that circumgalactic gas scatters Ly α photons which have escaped from the interstellar medium.

We suggest a physical analogy exists between the prominent Mg II $\lambda\lambda 2796.35, 2803.53$ P-Cygni line profiles recently discovered in near-UV spectra of star-forming galaxies (Tremonti et al. 2007; Martin & Bouché 2009; Weiner et al. 2009; Prochaska et al. 2011; Rubin et al. 2011; Erb et al. 2012) and the Ly α halos detected around higher redshift galaxies. The Mg II emission is prominent in bluer galaxies and galaxies with relatively low stellar mass (Martin et al. 2012), although further analysis indicates the strongest correlation with specific SFR (Kornei et al. 2013). These results appear consistent with the ideas that dust attenuation halts the escape of Mg II photons and outflows play a significant role in shaping the often-observed P-Cygni profiles.

Motivated by the need to improve empirical mass-loss rates and the discovery of Mg II emission around TKRS 4389 (Rubin et al. 2011, $z=0.69$), we examined the spatial extent of Mg II emission in LRIS spectra of individual, blue galaxies at $0.4 < z < 1.4$ included in the outflow census of Martin et al. (2012) and originally discovered by the Deep Extragalactic Evolutionary Probe 2 survey, DEEP2 (Newman et al. 2012). The spectrum of the outflow galaxy 32016857 resolves extended Mg II emission which we argue most likely reflects stellar continuum and H II region emission scattered by the outflow. We also describe extended Mg II emission around 32010773 and 12019973, two galaxies with spectra indicating the presence of outflowing gas (blueshifted resonance absorption and P-Cygni Mg II emission); but, in contrast to 32016857, the Mg II surface brightness profiles and kinematics can be fitted with either resonance scattering or direct emission from H II regions. Finally, the spectrum of 22028686 resolves resonance absorption across the galaxy, yet we detect the resonance emission over just one side of the galaxy, a situation which may provide insight into the conditions required for resonance emission to escape.

We use resonance scattering of the continuum light into our sightline to estimate mass-loss rates for 32016857 and TKRS 4389. To outline the physical argument, we consider spherical outflow geometries subtending a solid angle Ω . Continuum photons emitted at increasingly higher

frequencies (relative to the resonance) are absorbed by atoms at progressively larger radii if the radial velocity, $v(r)$, of the outflow increases outwards. At any radius, the spatial extent of the scattering region (over a fixed frequency range) grows with increases in the thermal or turbulent velocity. Provided the outflow density and the velocity component along the sightline do not change much over this interaction region, the computation of the scattering optical depth can be simplified using the Sobolev approximation (Sobolev & Gaposchkin 1960; Prochaska et al. 2011). Measurements of the extent of the scattering halo and the outflow velocity therefore effectively constrain the ionic density of the outflowing gas at a radius where the scattering optical depth is close to unity. We estimate the ionization correction by calculating the photoionization equilibrium and demonstrate how the clumpiness of the outflow affects the estimated mass-loss rate.

The paper is organized as follows. We review the data in Section 2 and present results for 32016857 in Section 3. In Section 4, we examine what galaxy properties favor scattered halo gas and present other examples of spatially extended emission-line gas from our study. We return to 32016857 in Section 5, where we use the Sobolev approximation to estimate the ionic gas density of the outflow, present the photoionization models, and discuss the implications for the mass-loss rate. An Appendix illustrates how the clumpiness of the warm phase of the outflow may affect the estimated mass-loss rate.

We adopt a Hubble constant of $H_0 = 70 \text{ km s}^{-1} \text{ Mpc}^{-1}$, and we assume a Λ CDM cosmology with $\Omega_M = 0.3$ and $\Omega_\Lambda = 0.7$. This cosmology yields a scale of $7.884 h_{70}^{-1} \text{ kpc}''$ at redshift $z = 0.9392$. We use vacuum wavelengths throughout to refer to both ultraviolet and optical transitions and atomic data from Morton (2003). Stellar masses and SFR's are derived assuming a Chabrier initial mass function (Chabrier 2003).

2. DATA

We previously described 208 Keck LRIS spectra of $0.4 < z < 1.4$ galaxies in Martin et al. (2012). Among the 145 spectra with both Mg II coverage and fitted Fe II resonance absorption, we have objectively searched for Mg II emission (Kornei et al. 2013). We use the parameters fitted to the Fe II absorption troughs in Martin et al. (2012) to describe the shape of the intrinsic Mg II absorption trough and definitively detect Mg II $\lambda\lambda 2796, 2803$ resonance emission in 22 spectra. A higher fraction of the spectra may have Mg II emission which is not uniquely separated from the absorption troughs.

The primary spectrum discussed in this paper, 32016857, was obtained on mask msc32aa (see Table 1 in (Martin et al. 2012)) using the configuration with the D560 dichroic, 600 l mm^{-1} blue grism blazed at 4000 \AA , and the 600 l mm^{-1} red grating blazed at 7500 \AA . Due to the non-photometric observing conditions for this mask, absolute flux calibrations for the blue and red spectra were obtained, respectively, by matching the DEEP2 photometry in the B and I bands, a procedure which also corrects the broad band luminosity for slit losses. This absolute flux calibration is less accurate than that derived from observations of standard stars under photometric conditions for most masks; however, all the LRIS

spectra have accurate relative fluxes independent of observing conditions. We refer the interested reader to Section 2.2 of Martin et al. (2012) for a more detailed description of the instrumental configuration, data acquisition, and spectral reduction.

To search for extended emission in the 2D spectral images, we fit a linear continuum through bandpasses to either side of the Mg II doublet. We visually inspected the 2D spectra both before and after continuum subtraction for any sign of Mg II emission. We collapsed the line emission (in both transitions) in the dispersion direction to create a surface brightness profile and compared it to the instrumental point-spread function (defined by a stellar spectrum). A similar procedure was followed to create an [O II] surface brightness profile from the red spectra. Finally, profiles of the continuum surface brightness were constructed from both the blue and red spectra directly adjacent to the emission line of interest.

3. CASE STUDY OF THE $Z = 0.9392$ GALAXY 32016857

In this section, we focus on the clearest example of spatially extended, scattered Mg II emission in our sample, 32016857. Figure 1 shows an image of this galaxy as well as the blue and red spectra obtained previously with LRIS. The R -band isophotes of 32016857 indicate a major axis roughly aligned with the position angle of the slit. However, the isophotes clearly show an asymmetry along the major axis which is not consistent with the projection of an inclined, symmetric disk. Higher resolution imaging is required to distinguish whether the major axis reflects the position angle of a disk or some more complicated morphology, such as two merging galaxies. We wish to emphasize, however, that the surface brightness distribution and kinematics of the [OII] emission are compatible with two emitting regions. In addition, we identify the object 5'' west of 32016857 in Figure 1a as 32016527 in the DEEP2 photometric catalog, which suggests the object is a compact galaxy based on its magnitude and color.

3.1. Galaxy Properties

Table 1 lists the measured properties of 32016857. It has notably blue $U - B$ color. The SFR estimated from the [O II] luminosity, as described in the notes to Table 1, is approximately $80 M_{\odot} \text{ yr}^{-1}$. The mass derived from the SED fit, $\log(M/M_{\odot}) = 9.82$ (Bundy et al. 2006), places 32016857 in the lowest tertile of the LRIS sample by stellar mass. This mass estimate should be accurate to within a factor of two because the K -band photometry of 32016857 directly constrains the rest-frame, near-IR continuum. At $z \approx 1$, abundance matching places galaxies with stellar mass $\log M_{*}/M_{\odot} = 9.8$ in halos of total mass $\log M_h/M_{\odot} \approx 11.5$ (Behroozi et al. 2010), consistent with the clustering of DEEP2 galaxies which places galaxies brighter than $M_B < -20.77$ in halos more massive than $\log M_h/M_{\odot} = 11.3$ (Coil et al. 2008). In numerical simulations, halos with masses similar to our best estimate for 32016857 (specifically $M_h < 10^{12} M_{\odot}$), gas accretion is dominated by the cold flows never shock-heated to the halo virial temperature (e.g., Kereš et al. 2005).

In the red side spectrum, shown in panel b of Figure 1, the resolution of 220 km s^{-1} FWHM does not quite resolve the prominent [O II] $\lambda\lambda 3727.09, 3729.88$

emission lines. The blue spectrum, 282 km s^{-1} FWHM resolution, reveals strong emission in the Mg II $\lambda\lambda 2796.35, 2803.53$ doublet with a P-Cygni profile (bottom panels). The recombination lines from hydrogen and helium as well as the strong emission in the C II] $\lambda 2324 - 29$, C III] $\lambda 1908.73$, [Ne III] $\lambda 3869.85, \lambda 3968.58$, and [O II] lines come from H II regions photo-ionized by massive stars. The absence of [Ne V] $\lambda 3426.98$ emission argues against an AGN as the dominant source of ionizing radiation.

The emission lines in the red spectrum dominate the cross-correlation signal with template spectra and thereby determine the LRIS redshift of $z = 0.9392$. The root-mean-square (RMS) error in the dispersion solution of the red spectrum is only a few km s^{-1} ; hence the RMS error in the blue dispersion solution, about 18 km s^{-1} , determines the systematic uncertainty in the relative velocities of the low-ionization absorption and nebular emission. In the blue spectrum, the centroid of the C III] emission line lies just $-30 \pm 31 \text{ km s}^{-1}$ from the intercombination transition which dominates the emission at high density. We readily acknowledge a larger discrepancy of 50 km s^{-1} between the LRIS redshift and the DEEP2 survey redshift, likely caused by differences in slit position angle but irrelevant to the value of relative velocities between the absorption lines and nebular emission.

The absorption lines in the LRIS spectrum are not sufficiently resolved to measure the maximum blueshift from the Fe II line profiles. The fitted centroid of the Fe II absorption lines is blueshifted $V_1 = -91 \pm 15 \text{ km s}^{-1}$ (Martin et al. 2012). The projected outflow velocity is more accurately estimated by the two-component fit shown in the right column of Figure 2. Correcting for the interstellar absorption at the systemic velocity increases the blueshift of the Doppler component to $V_{Dop} = -227 \pm 82 \text{ km s}^{-1}$.

While the $\lambda 2803$ absorption trough may be filled in by emission from both Mg II transitions, only $\lambda 2796$ emission fills in the intrinsic $\lambda 2796$ absorption trough. In Mg II $\lambda 2803$, Figure 1 shows absorption blueward of the systemic velocity and redshifted emission. The marginally-resolved emission wing extends to $+310 \text{ km s}^{-1}$ (Martin et al. 2012). The corresponding red wing of the Mg II $\lambda 2796$ profile may significantly fill in the bluest portion of the intrinsic $\lambda 2803$ absorption profile. Emission at the systemic velocity in both transitions likely fills their intrinsic absorption profiles at the systemic velocity.

Optically thick Mg II absorption will produce an intrinsic $\lambda 2803$ trough with the same equivalent width as the $\lambda 2796$ trough which is twice as strong in the optically thin limit. Remarkably, however, the absorption equivalent width of the Mg II $\lambda 2796$ absorption trough is less than that in $\lambda 2803$ as seen in both Figure 1 and Table 2. While low S/N ratio could produce such an effect through measurement error, our analysis suggests a different interpretation. We can understand the net Mg II profile provided the intrinsic ratio of emission-line strengths $W_{em}(\lambda 2796)/W_{em}(\lambda 2803)$ exceed the ratio of absorption-line strengths $W_{abs}(\lambda 2796)/W_{abs}(\lambda 2803)$. In support of this approach, we note that in Table 2 the net emission equivalent width of the stronger Mg II transition, $-2.13 \pm 0.29 \text{ \AA}$, is higher than in the weaker Mg II

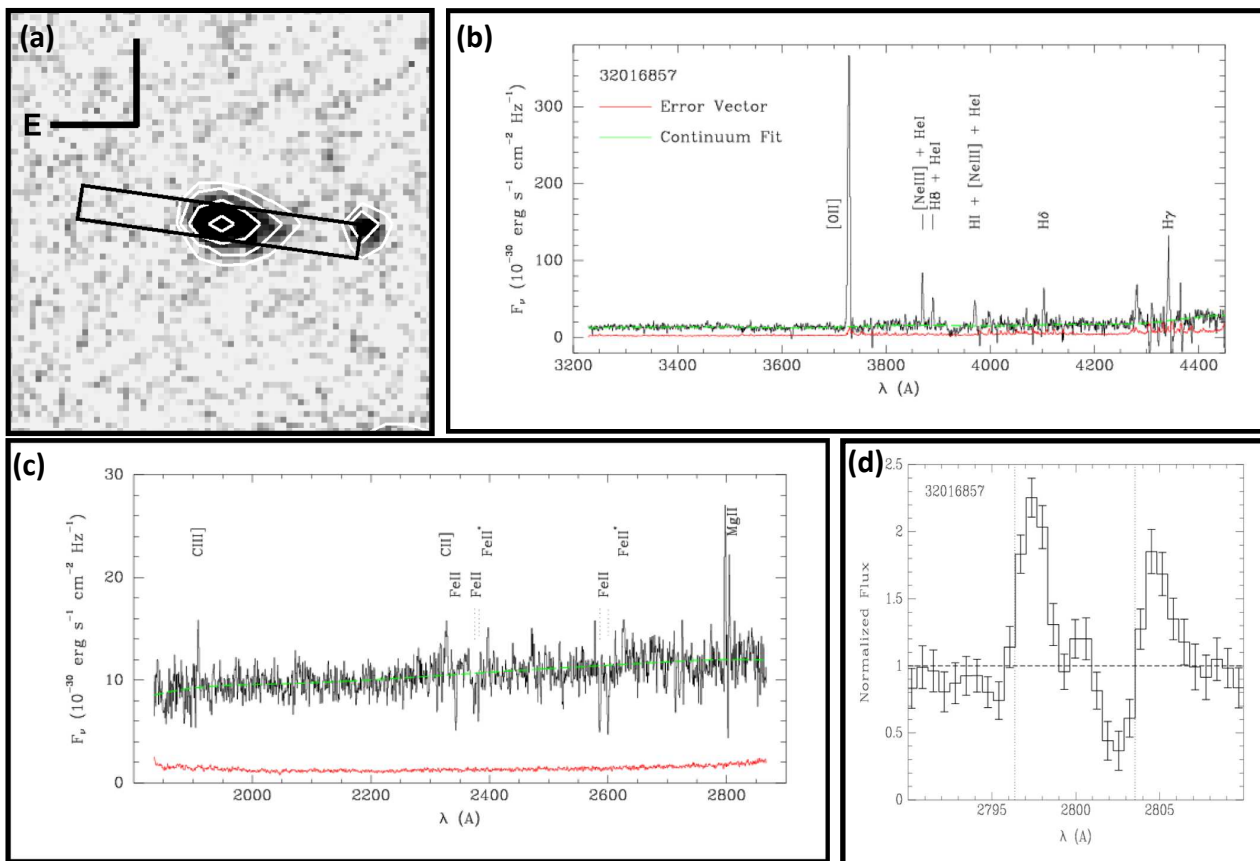


FIG. 1.— (a): CFHT *R*-band image of 32016857 from Coil et al. (2004). Contours, spaced by a factor of two in surface brightness, show an elongated structure; and the slit ($PA = 82.0^\circ$; $10''.0$ long by $1''.2$ wide) runs roughly along the major axis of the galaxy. The surface brightness profile along the major axis, however, is clearly more extended to the west than to the east. Due to this asymmetry, an inclined disk does not describe the morphology well, and the position angle of the semi-minor axis need not indicate the direction of the projected rotation axis. (b): Red spectrum of 32016857 showing strong lines and fitted continuum level. The strong nebular line emission determines the systemic velocity, $z = 0.939196$. Table 2 provides the transition wavelengths. (c): Blue spectrum of 32016857 showing strong absorption lines from Fe II, C II] emission, Mg II emission, Fe II* emission, and fitted continuum level. The continuum S/N ratio at 2450 \AA is 8.3 per pixel. Table 2 provides the transition wavelengths. (d): Integrated spectrum of 32016857 zoomed in to illustrate the P-Cygni-like line profile of the Mg II doublet. Dotted, vertical lines denote the systemic velocity, and the dashed line marks the normalized continuum level.

line at $\lambda 2803$. Qualitatively at least, we can therefore create a line profile with a weak $\lambda 2796$ trough (relative to $\lambda 2803$) if the intrinsic absorption troughs are both saturated and therefore equal in area.

To explore this solution quantitatively in a manner that fully incorporates the spectral S/N ratio, we fit a model consisting of an emission doublet simply added to the intrinsic absorption troughs. This model assumes the emission region lies beyond most of the absorbing gas. The caption of Figure 3 describes the functional form of these components. We wrote a custom Markov Chain Monte Carlo fitting code in Python to explore the range of possible parameter values. The fit shown in Figure 3 illustrates a typical fit drawn from the Markov chain.

To estimate the values of the absorption and emission components, we used the posterior probability distributions compiled for each parameter from the full Markov chain to determine the mean values of the parameters and their 1σ uncertainties. Our fit describes the absorption troughs with a Doppler shift of $V_{abs} = -11^{+51}_{-49} \text{ km s}^{-1}$, Doppler parameter $b_{Dop} =$

$81^{+23}_{-24} \text{ km s}^{-1}$, covering factor $C_f = 0.91^{+0.06}_{-0.12}$, and optical depth at line center $\tau_0 = 68^{+80}_{-44}$; it finds an emission component with a redshift of $V_{em} = 105^{+12}_{-10} \text{ km s}^{-1}$, width $\sigma = 14^{+14}_{-9} \text{ km s}^{-1}$, amplitude $A_{2796} = 4.74^{+0.77}_{-0.81}$ for the $\lambda 2796$ transition, and doublet ratio $A_{2796}/A_{2803} = 1.51^{+0.20}_{-0.16}$. We find that the intrinsic absorption troughs typically have very similar equivalent widths. In contrast, only doublet ratios A_{2796}/A_{2803} , near 1.5 provide acceptable descriptions of the emission. We conclude that the optical depth of the emission region in our slit is lower than that of the absorbing gas along our sightline. We interpret the difference between the absorption and emission doublet ratios as an indication that different physical regions of the galaxy produce the emission and absorption – e.g., non-spherical geometries for the scattering region and/or significant Mg II emission from H II regions.

The net Fe II absorption troughs more nearly reflect the intrinsic shape of the absorption profile than does Mg II absorption. The resonance emission that fills in these troughs may be generated by H II re-

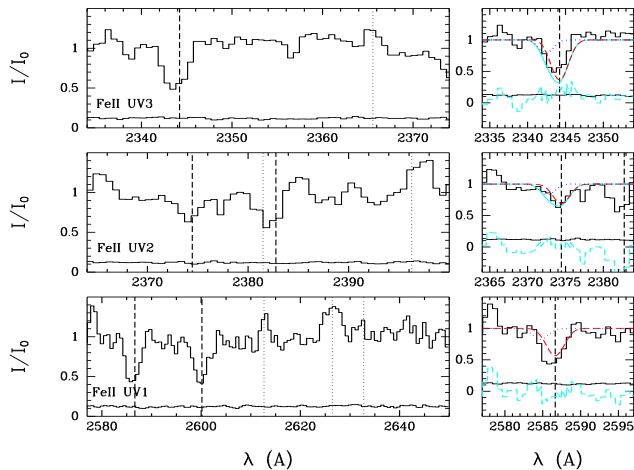


FIG. 2.— Continuum normalized spectrum showing the near-UV, Fe II multiplets UV1, UV2, and UV3. *Left column:* The vertical dashed (dotted) lines mark the Fe II (Fe II*) transitions listed in Table 2. The 3σ upper limit on the equivalent width of the Fe II 2261 line, not shown, is 0.60\AA (Martin et al. 2012). Fluorescent emission from the upper level of the $\lambda 2600$ transition ($z^6 D_{9/2}^0$) is detected at $\lambda 2626$, and the marginal detections of both Fe II* $\lambda 2612$ and $\lambda 2632$ mark fluorescent decays from the $z^6 F_{7/2}^0$ level, which is excited by absorption in $\lambda 2587$. A net excess of emission is also detected near the wavelength of the Fe II* $\lambda 2396$ transition in UV2 and at Fe II* $\lambda 2365$ in UV3. While Table 2 shows that many of these detections are not individually robust statistically, the combination of features clearly argues for strong fluorescent emission in the spectrum of 32016857. *Right column:* Two-component joint fit (solid) to the Fe II λ 2344, 2374, and 2587 transitions. The Doppler component (blue, dotted line) has a blueshift of $V_{Dop} = -227 \pm 82 \text{ km s}^{-1}$ and an equivalent width $W_{Dop}(\lambda 2374) = 0.41\text{\AA}$. Fit residuals (dashed) are shown relative to the error spectrum at the bottom of each plot.

gions or created by the absorption of continuum photons in the surrounding gas. As emphasized in Erb et al. (2012), H II regions produce much more emission in Mg II than in Fe II, so nebular emission will have a proportionately larger impact on the shape of the net Mg II line profile. In our integrated spectra of 32016857, the flux ratio of the [O II] and Mg II emission, $F([\text{O II}] \lambda\lambda 3726, 29)/F(\text{Mg II } \lambda 2796) \approx 42$ (uncorrected for reddening), is consistent with line ratios calculated for nebulae at slightly sub-solar metallicity photoionized by a starburst spectral energy distribution. For example, comparison of this line ratio to Figure 16 in Erb et al. (2012), indicates an ionization parameter $\log U \gtrsim -2.9$, where the lower limit indicates that the reddening-corrected line ratio would require a larger ionization parameter. In addition, in contrast to the ground state of Mg II, which is a singlet, the ground-state of Fe II has fine structure. In Fe II, absorption of a resonance photon is often followed by the emission of a longer wavelength photon (Rubin et al. 2011; Prochaska et al. 2011; Martin et al. 2012). This fluorescent emission, clearly visible in Figure 2 near the systemic velocity, does not fill in the resonance absorption troughs.

Table 2 summarizes the equivalent widths and velocities of Fe II absorption troughs and Fe II* emission. The relative strengths of the individual absorption lines are not well fit with standard curve-of-growth techniques due to differential amounts of emission filling. Using the two-component fit shown in Figure 2, Martin et al. (2012)

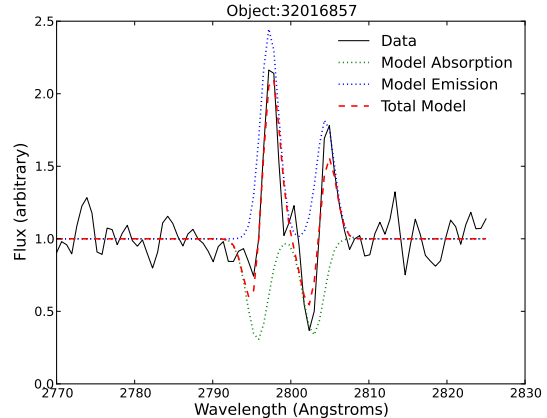


FIG. 3.— Typical example of a fit to the Mg II complex in the 32016857 spectrum. We model the emission with two Gaussian line profiles sharing a common Doppler shift and velocity width but independent amplitudes. We add the emission component to the fitted absorption doublet described by $I(\lambda) = 1 - C_f + C_f \exp(-[\tau_{2796}(\lambda) + \tau_{2803}(\lambda)])$, where the optical depth in the bluer line is twice that of the redder line at the same Doppler shift; and a Gaussian distribution describes the variation in optical depth with Doppler shift, $\tau(\lambda) = \tau_0 \exp(-[(\lambda - \lambda_0)/(\lambda_0 b/c)]^2)$. We convolve this joint model with a Gaussian function describing the instrumental resolution. The example shown here fit the absorption troughs with a Doppler shift of $V_{abs} = -104 \text{ km s}^{-1}$, Doppler parameter $b_{Dop} = 70_{-24}^{+23} \text{ km s}^{-1}$, covering factor $C_f = 0.97$, and optical depth at line center $\tau_0 = 15$; it describes the emission lines with a Doppler shift of $V_{abs} = 70 \text{ km s}^{-1}$, width $\sigma = 79 \text{ km s}^{-1}$, amplitude $A_B = 1.67$ for the $\lambda 2796$ transition, and doublet ratio $A_B/A_R = 1.67$. The doublet ratio fitted to the emission component is larger than that of the absorption component.

estimate the ionic column density of the Doppler component lies in the range $\log[N_{Dop}(\text{Fe}^+)C_f(\text{cm}^{-2})] = 14.42 - 15.53$, where C_f is a gas covering factor of order unity.

3.2. Emission Line Properties along the Slit

The two dimensional (2D) spectra of 32016857 constrain the spatial extent of the emission regions. Figure 4 compares the structure of the Mg II and [O II] line emission. While the Doppler shift of the [O II] emission shifts by approximately 190 km s^{-1} over 17 kpc along the slit, no velocity gradient is detected in Mg II emission. While the H II regions producing the [O II] emission probably contribute to the total Mg II emission, based on the kinematic differences between the 2D spectra, we suggest that the Mg II emission takes on the velocity of the outflowing material, not the velocity of the H II regions, because it is scattered by halo gas.

Figure 5 compares the emission profiles along the slit. The continuum emission, rather than showing the symmetric profile of an inclined disk, shows an extended feature to the west with strong [O II] but no Mg II emission. The [O II] emission is unresolved to the east. In contrast to this nebular line emission, the Mg II surface brightness profile is spatially extended to the east but unresolved to the west. The opposite directions of the extended [O II] and Mg II emission along the slit suggest distinct physical origins.

The Mg II surface brightness averaged over a spatial resolution element (six pixels) 10.6 kpc eastward of the galaxy is 3.1 standard deviations above the background. The continuum emission is also spatially extended to the

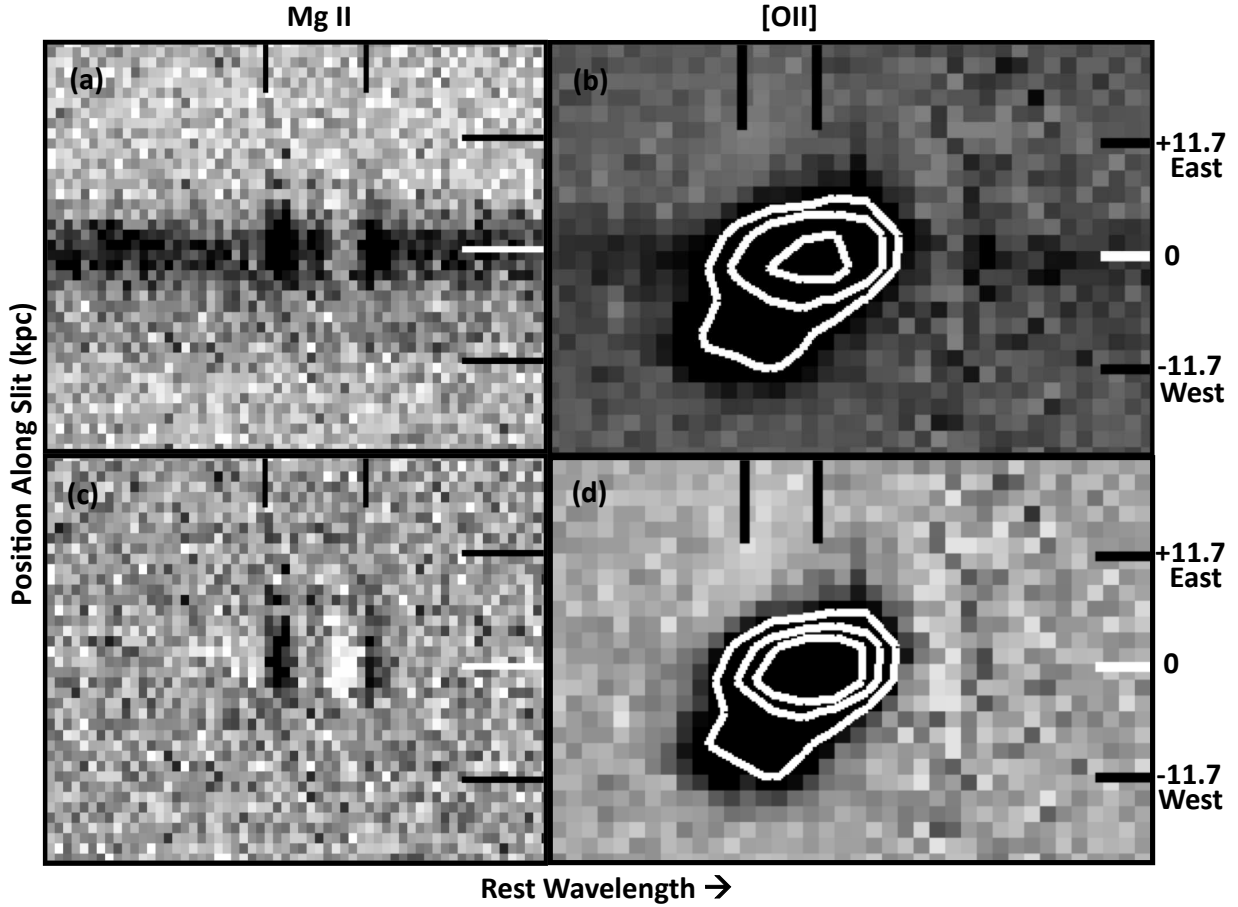


FIG. 4.— The 32016857 spectrum near Mg II and [O II]. (a) The Mg II $\lambda\lambda 2796.35, 2803.53$ doublet (vertical lines separated by 770 km s^{-1}) is detected in emission and absorption. (b) The [O II] $\lambda\lambda 3727.09, 3729.88$ doublet (vertical lines separated by 225 km s^{-1}) is detected in emission. (c) Continuum subtracted Mg II spectrum. (d) Continuum subtracted [O II] spectrum. Linearly spaced contours show a velocity gradient along the slit which we attribute to the rotation of the galaxy.

east. Averaged over the same spatial resolution element at 10.6 kpc, the line emission is marginally, 2.1σ , more significant than the continuum emission indicating the line emission is likely more extended than the continuum emission. The Mg II emission is not spatially resolved to the west.

To estimate the radial extent of the Mg II emission, we introduce a simple model for the surface brightness profile measured along the slit inspired by, but different in detail from, the approach used by Rubin et al. (2011) to model the galaxy TKRS 4389. The emission model includes an H II region component and an extended component. The normalized [O II] surface brightness profile determines the shape of the H II component. Since the observed Mg II profile is spatially resolved to the east but not to the west, we require an asymmetric extended component. We adopt a semi-circular emission region of constant surface brightness. The radius, R_C , of the extended emission describes the projected distance from the center of 32016857, and the straight-side of the semi-circle is perpendicular to the slit. This 2D model of the surface brightness profile is convolved with a Gaussian model of the atmospheric seeing, $FWHM = 0''.8$ and then “observed” through a $1''.2$ slit. In analogy with Ly α

radiative transfer, photons scattered off the far side of the outflow escape as redshifted emission.

We explore 14 values of R_C from 4.9 to 35.9 kpc, corresponding to an angular extent of $0''.621$ to $4''.554$ along the slit. For each model of the extended emission, we fit the Mg II surface brightness profile with a linear combination of the H II and extended components. Figure 6 shows the minimum residuals at $R = 11.4$ kpc, where the separation between models is about 0.34 kpc. The extended component and the H II component determine the net surface brightness profile to the east and west, respectively, in Figure 6. For the best-fit model, the eigenvalues of the two components are similar, and the extended component contributes 46% of the total Mg II flux. While the residuals show that this model provides a reasonable description of the data, it does not tightly constrain the radius of the scattering halos. Smaller halos cannot be excluded with high confidence due to the profile smearing caused by atmospheric turbulence, and this blurring also means the reduced chi-square values increase slowly with increasing halo radius.

4. GALAXIES WITH HALOS OF SCATTERED EMISSION

Spectra of about 20% of star-forming galaxies at $z \sim 1$ show resonance absorption at large ($\gtrsim 100 \text{ km s}^{-1}$)

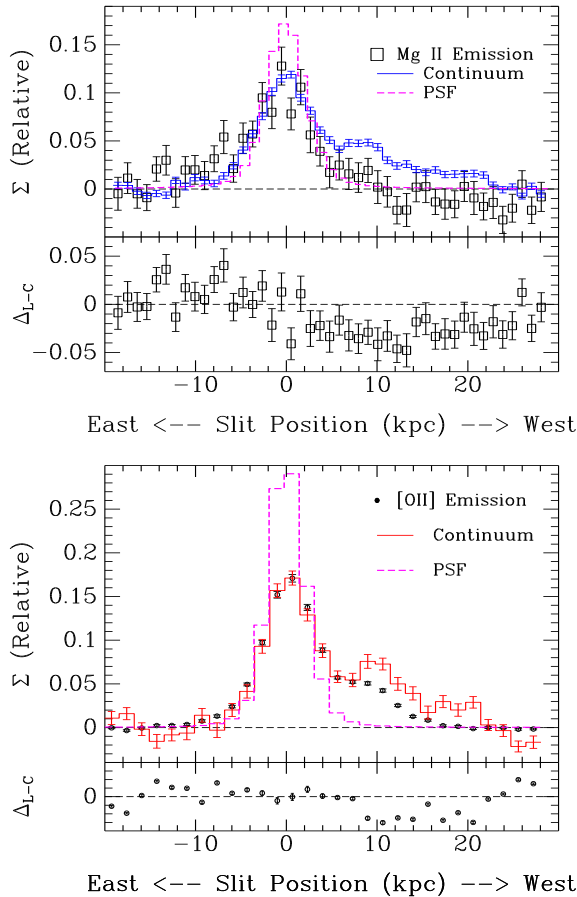


FIG. 5.— Surface brightness profiles across 32016857. The line emission is normalized to unity. To facilitate comparison to the emission line profile, the continuum has been scaled to match the maximum line emission. The residuals in the bottom panels show the difference of these scaled line and continuum profiles along the slit. The point spread function (psf) was measured from a stellar spectrum and has been normalized to unity area. *Top:* The Mg II doublet emission is spatially extended to the east, as can be seen from the comparison to the stellar profile. At -10.6 kpc, the average Mg II surface brightness over one resolution element (6 pixels) is significantly (3.1σ) above the background. The continuum emission is also extended towards the east. In the lower panel, which shows the difference between the normalized line and continuum profiles, the line emission is marginally (2.1σ) more extended than the continuum emission. *Bottom:* In contrast, the [O II] surface brightness profile is not spatially resolved to the east but is well resolved to the west. Since the spatial distribution of the Mg II emission does follow that of the [O II] emission, the former clearly does not come directly from H II regions.

blueshifts relative to nebular and stellar lines (Martin et al. 2012). Since the properties of star-forming galaxies with and without blueshifted absorption do not differ very significantly, the absence of blueshifted resonance absorption in some spectra has been attributed to the collimation of the outflows. A bipolar flow, for example, produces a blueshift in the spectrum when the orientation of the galactic disk is face-on and the starlight passes through the near side of the outflow cone. This interpretation of the blueshifted fraction suggests outflows are a generic property of star-forming galaxies at intermediate redshift and raises the question of why scattered emission is not detected more frequently.

Many properties of 32016857 and TKRS 4389 (Rubin et al. 2011), the only other distant galaxy detected in extended Mg II emission, are similar. In particular, Rubin

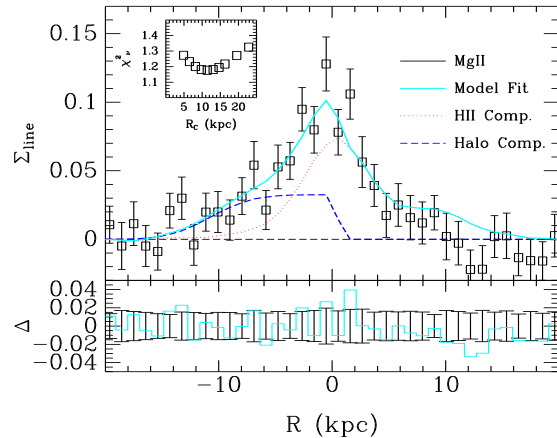


FIG. 6.— The normalized Mg II surface brightness profile with fitted model (cyan line). This particular model, while not necessarily unique, provides an acceptable description of the Mg II surface brightness with fit statistic $\chi^2_{\nu} = 1.18$. The model is a linear combination of the emission from an HII region component (red, dotted line) and an extended halo (blue, dashed line). The normalized [O II] surface brightness profile defines the HII region component. The extended component is modeled by a semi-circular region of radius R_C and constant surface brightness. The best-fit radius for this scattered component is $R_C = 11.4$ kpc, and the spacing between models is 0.3 kpc. The lower panel shows that the errors in the data values are comparable in magnitude to the residuals from the fit (data minus model). The inset, however, shows the reduced chi-square values over a large range in R_C . Since the range in R_C over which χ^2 increases by 1 from its minimum value at 11.4 kpc is quite large, models with halo radii considerably smaller or larger than 11.4 kpc are not ruled out.

et al. (2010) suggest that TKRS 4389 is exceptionally bright for its redshift of $z = 0.6943$. It is slightly bluer and more luminous than 32016857 and has about three times as much stellar mass. A rough estimate for the SFR is $\approx 80 M_{\odot} \text{ yr}^{-1}$. The deepest parts of the Fe II absorption troughs are blueshifted roughly 200 km s^{-1} . An HST image of TKRS 4389 shows signs of recent merger activity. Rubin et al. (2010) cite the weak [Ne V] emission, $W_r = -0.84 \pm 0.1 \text{ \AA}$, as evidence that TKRS 4389, in contrast to 32016857, hosts a low-luminosity active galactic nucleus (AGN).

The very blue colors of 32016857 and TKRS 4389 are typical of Mg II emitters, which have lower masses, bluer colors (i.e., less reddening), and higher sSFR than the average star-forming galaxy at intermediate redshifts (Erb et al. 2012; Martin et al. 2012, Rubin et al., in prep). However, these two galaxies are more luminous than the average Mg II emitter; their blue luminosities fall in the highest tertile of the Martin et al. (2012) sample. In spite of the high luminosity of 32016857, its stellar mass falls in the lowest tertile of our sample. The mass of TKRS 4389 is significantly higher, near the upper bound of our middle tertile. Galaxies that are both as luminous and as blue as 32016857 are rare. Only 9 of 208 galaxies in the parent sample have $U - B < 0.459$ and $M_B - 5 \log h_{70} < -21.3$. Three of these 9 galaxies are Mg II emitters by the definition of Kornei et al. (2013), but only the 32016857 spectrum shows spatially extended Mg II emission.

Many factors, including the size of the spectroscopic aperture, the solid angle of the outflow and spectroscopic aperture, the amount of interstellar gas and dust, and the orientation of the galaxy and wind affect whether an out-

flow can be detected in resonance emission. Accordingly, it is unclear whether the resonance photons only escape from these galaxies or whether the emission is otherwise spread over too large a solid angle to detect it through a narrow slit. Drawing from our observation that both 32016857 and TKRS 4389 have uncommonly large luminosities, mapping Mg II emission in and around galaxies like these nine may be the most direct way to determine whether scattered halo emission is a generic property of intermediate redshift galaxies. While this could be accomplished with LRIS using additional longslit position angles, the next generation of optical spectrographs with large integral field units, particularly KCWI at Keck and MUSE at VLT, will be well positioned to characterize the halo emission.

With the aim of better informing these future investigations, we describe in Section 4.1 additional highlights from our investigation of the spatial extent of Mg II emission in deep, LRIS spectra. From the union of a color selected sub-sample and the sample selected by Mg II emission in the integrated spectra, we identified two more (for a total of three) examples of extended Mg II emission which we discuss in this section. We also describe a noteworthy example of extended Mg II absorption with unresolved emission in 22028686. Finally, in Section 4.2, we remark on the absence of Fe II λ 2383 emission. We return to 32016857 in Section 5 where we discuss the implications of scattered Mg II emission for mass-loss rates. The reader primarily interested in the physical properties of outflows rather than the challenge of detecting scattered emission should proceed directly to Section 5.

4.1. Additional Examples of Spatially Resolved Mg II Structure

The bluest fifth of the Martin et al. (2012) sample contains 42 galaxies with $U - B < 0.459$ and is of particular interest since the Mg II emitters tend to have blue colors (Martin et al. 2012; Kornei et al. 2013). All but 4 of these spectra cover the Mg II doublet, yet only 10 of these 38 show prominent Mg II emission in integrated spectra. Among this subsample, we found only two examples of spatially extended emission in the Mg II doublet. In addition to 32016857, the Mg II emission in our spectrum of 32010773 is spatially extended.

Figure 7 shows the surface brightness profiles of the Mg II emission (panel d), blue continuum, [O II] emission (panel c), and red continuum along the slit crossing 32010773. In contrast to the surface brightness profiles measured across 32016857, the Mg II emission across 32010773 is no more extended than the blue continuum emission. In the continuum-subtracted, 2D spectra, the velocity gradients of the Mg II and [O II] emission along the slit do not obviously differ, so the Mg II emission may come directly from H II regions. Our data do not require (nor do they rule out) scattered Mg II emission. This galaxy does clearly have an outflow; the large blueshift of the Fe II resonance lines, $V_1 = -198 \pm 46 \text{ km s}^{-1}$, is quite significant. The color of 32010773, $U - B = 0.23$ is among the bluest in the sample; but the luminosity of 32010773, $M_B - 5 \log h_{70} = -20.68$, is much lower than the luminosity of either 32016857 or TKRS 4389. The absence of resonance emission that is clearly extended relative to the continuum around 32010773 is consistent with the conjecture that detection of a scattering halo

requires especially luminous galaxies.

In addition to these 10 Mg II emitters with very blue color, Kornei et al. (2013) identified 12 more Mg II emitters in the Martin et al. (2012) sample with $U - B$ redder than 0.459. Among these redder Mg II emitters, we found spatially extended Mg II and continuum emission across 12019973. Figure 8 shows the variation in the Mg II and [O II] emission along the slit. Across 12019973, much like 32010773, the surface brightness profile of the line emission is no more extended than the continuum emission, neither proving nor ruling out scattering by an outflow. We note that the Doppler shift of the Fe II resonance lines, $V_1 = -59 \pm 28 \text{ km s}^{-1}$, provides marginal evidence for an outflow from this galaxy. The color, $U - B = 0.539$, and stellar mass, $\log(M/M_\odot) = 10.15$, of 12019973 are typical of the sample. This galaxy has a relatively low luminosity, $M_B - 5 \log h_{70} = -20.57$, which may contribute to the faintness of any extended halo.

Figure 9 shows the 2D spectra of another Mg II emitter, 22028686, a star-forming galaxy with $U - B > 0.459$. Although the Mg II emission is not spatially resolved, the resonance absorption troughs extend well beyond the emission region. The Mg II absorption lines are tilted in the opposite sense of the velocity gradient indicated by the [O II] Doppler shifts along the slit. Since the [O II] emission defines the systemic redshift, the redshifted and blueshifted [O II] emission to the northeast and southwest of the galactic center reveal either the projected rotation of the galaxy or the orbital motion of two merging galaxies. The centroid of the Mg II absorption to the southwest of the galaxy is consistent with the velocity of the blueshifted side of the galaxy. It is the even larger blueshift of the Mg II absorption centroid to the northeast that makes the absorption lines tilt in the opposite direction of the [O II] emission. Where the Mg II absorption is blueshifted on the northeastern side of the galaxy, we detect strong resonance emission at redshifted velocities. No resonance emission is detected along the south-western half of the slit. We note that the Fe II absorption in the integrated spectrum does not show a net Doppler shift, $V_1 = -1.9 \pm 9.2 \text{ km s}^{-1}$. Much of the shift in the centroid of the Mg II absorption may therefore be caused by variations in emission filling along the slit, and the spatial gradient in the absorption velocity likely does not reflect galactic rotation.

The detection of Mg II emission from just a portion of the absorbing region in 22028686 may help illuminate the physical conditions required for the resonance emission to escape the galaxy. To gain this insight, we review studies which have mapped Na I resonance absorption across galaxies. As illustrated for example by spectral mapping of NGC 1808 (Phillips 1993) local ULIRGs (Martin 2006), and Mrk 231 (Rupke et al. 2005; Rupke & Veilleux 2011), the absorption from outflows is not redshifted anywhere across the galaxy because the absorbing gas must lie in front of the continuum source. Across local ULIRGs, the Na I velocity gradient is very similar to the slope of the rotation curve, but the absorption trough is highly blueshifted everywhere along the slit. This situation would be expected if the outflow was launched from a rotating disk, and we might expect a small velocity gradient in the absorption Doppler shift (not seen) comparable to the tilt of the nebular emission lines. In spite of the very limited spatial resolution across

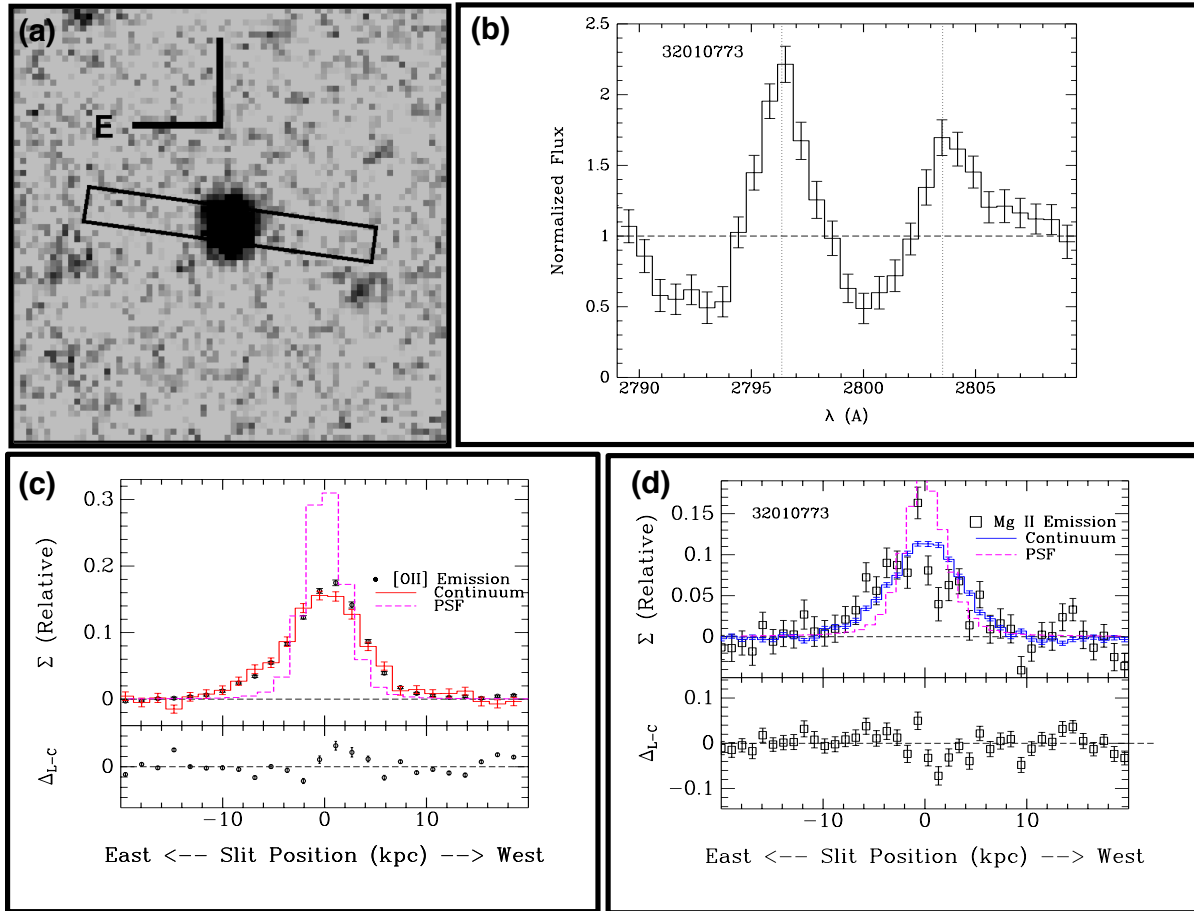


FIG. 7.— Observations of 32010773. (a) The galaxy, shown in a CFHT R-band image, was observed with LRIS through a $1''.2$ by $10''.0$ slitlet at a position angle of 82.0° (on mask msc32aa as described in Table 1 of Martin et al. (2012)). (b) The blue LRIS spectrum reveals a P-Cygni Mg II profile. (c) Normalized surface brightness profiles of the [O II] emission and continuum are spatially extended relative to the point-spread function. (d) Normalized surface brightness profiles of the Mg II emission is partially resolved but no more spatially extended than the blue continuum emission. The Gaussian FWHM fitted to the Mg II surface brightness profile, $1''.25 \pm 0''.11$, is not significantly larger than the FWHM of the blue continuum profile, $1''.14 \pm 0''.02$. The fitted centroid of the Mg II emission profile is 1.2 pixels ($0''.16$) east of the continuum centroid, a 2.9σ discrepancy in position.

22028686, we speculate that the geometry might instead mimic NGC 1808 where differences in extinction shape the resonance line profile of the outflow. As illustrated in Figures 1 and 4 of Phillips (1993), the blueshifted lobe of the outflow is detected in absorption across the inclined disk. Resonance emission is detected from the far side of the outflow where it pokes out from behind the disk but plumes of dust visible on the near side of the outflow at the location of the slit presumably destroy the resonance photons. Hence the implication from the 22028686 spectrum seems to be that the sightline towards the absorbing gas on the northeast side encounters less dust than that towards the southwest side of the slit. Higher resolution imaging could confirm the presence of a disk, determine the disk orientation, and perhaps reveal the locations of dust filaments in this galaxy.

In summary, among 145 spectra with coverage of the Mg II doublet, including 50 galaxies with either prominent Mg II emission or very blue $U - B$ color, we find only three examples of spatially resolved Mg II emission: 32016857, 32010773, and 12019973. Our analysis of 32016857 doubles the number of known galaxies with

Mg II emission extending beyond the stellar continuum. With only two examples where the extended emission must be scattered, we can only begin to speculate about the conditions producing scattered Mg II halo emission. However, since the unique properties of 32016857 and TKRS 4389 are their high luminosities (for their blue color), we suggest that large luminosities are essential to raise the surface brightness of the scattered emission to detectable levels. Further support for the idea that most scattering halos are below current detection limits comes from stacking the surface brightness profiles of $1 < z < 2$ Mg II-emitting galaxies; their Mg II emission is marginally more extended than the near-UV continuum at radii of $0''.8$ (Erb et al. 2012).

4.2. Absence of Extended Emission in Fe II Lines

Our spectrum of 32016857 shows prominent fluorescent emission in Figures 1 and 2. We did not find extended emission in resonance lines of Fe II or fluorescent Fe II* lines nor did Rubin et al. (2011) in their TKRS 4389 spectrum. The Fe II $\lambda 2383$ absorption is optically thick in most galaxy spectra; under LS coupling, the only

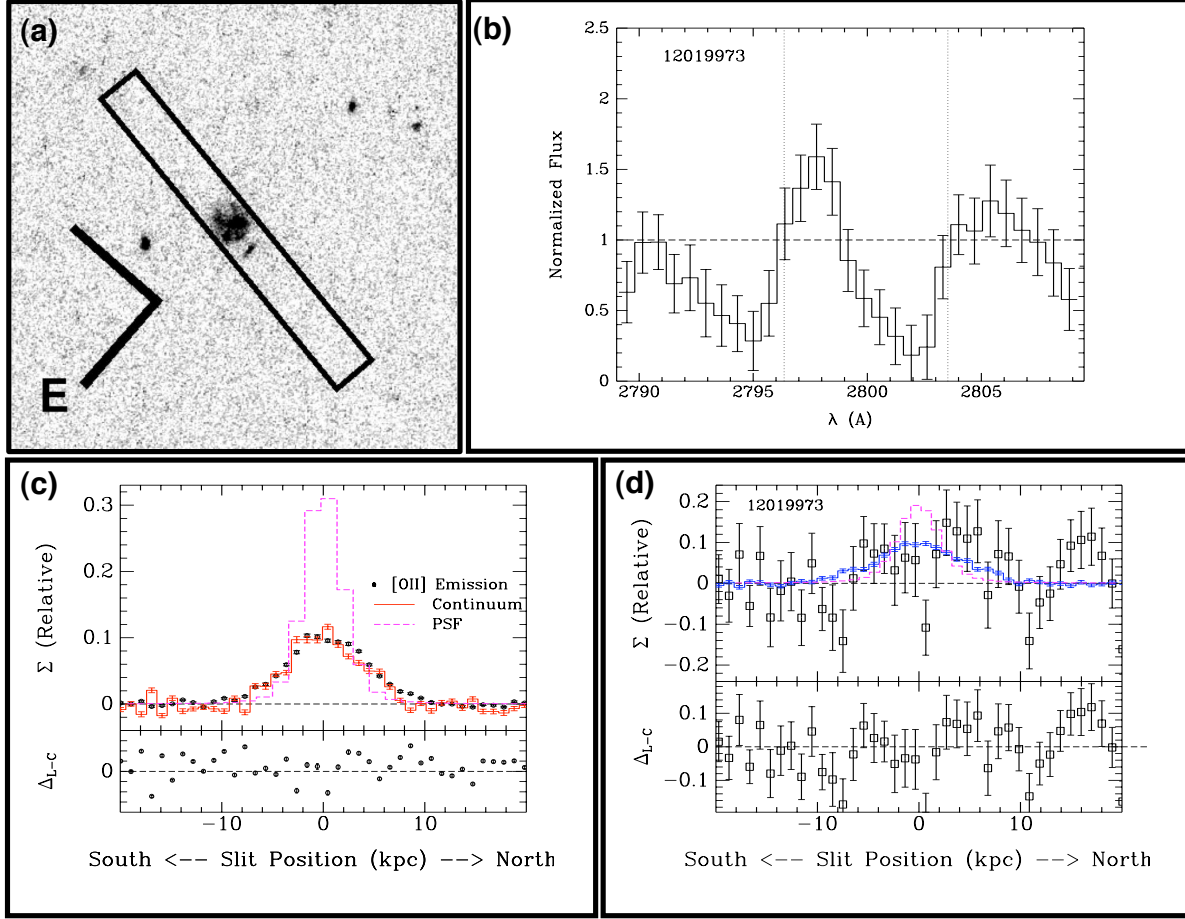


FIG. 8.— Observations of 12019973. (a) The galaxy is shown on the V band HST image described in Kornei et al. (2012). We obtained the LRIS spectrum through a $1''.2$ by $10''.0$ slitlet at a position angle of 170.0° (on mask msc12ee as described in Table 1 of Martin et al. (2012).) (b) The blue LRIS spectrum reveals a P-Cygni Mg II profile. (c) Along the slit, the strong [O II] emission is slightly more extended than our model of the psf but not significantly more extended than the red continuum emission. (d) The Mg II surface brightness profile exemplifies the low S/N ratio typical of Mg II emission.

permitted decay from the upper energy level, here the excited $z^6F_{11/2}^0$ state of Fe^+ , is to the ground $a^6D_{9/2}$ state. The absence of Fe II $\lambda 2383$ emission in spectra with prominent Mg II $\lambda 2803$ emission is at first surprising considering the similar oscillator strengths of the $\lambda 2383$ and $\lambda 2796$ transitions and the (only) 20% larger cosmic abundance of magnesium (relative to iron).

Several factors may contribute to the paucity of Fe II $\lambda 2383$ emission. A greater depletion of iron (relative to magnesium) onto grains, for example, may reduce the Fe II $\lambda 2383$ optical depth relative Mg II $\lambda 2803$. In the Milky Way, however, the relative depletion of Fe and Mg in the halo clouds is much lower than the ratio measured for disk clouds (Savage & Sembach 1996). Hence, we might anticipate a similar depletion of Fe and Mg onto grains in outflows. Alternatively, since iron is not a light element, deviations from pure LS coupling might in principle allow decay to another term thereby reducing the resonance emission (Shull, pvt. comm.), but we find no observational evidence for unidentified emission lines in support of this conjecture in the near-UV spectra. Third, as suggested recently by Erb et al. (2012), boosting the Mg II emission, rather than suppressing the Fe II emission, offers another explanation. Those authors

show that photoionized gas produces more emission in Mg II than Fe II, so emission from H II regions may boost the intensity of the scattered Mg II radiation relative to the scattered Fe II photons.

The most important factor driving this discrepancy, however, appears to be the ionization corrections. Gialavalis et al. (2011) show (see their Figure 14) that photoionization models of very low column density ($N_H \sim 10^{18} \text{ cm}^{-2}$) gas indicate a large plausible range in the relative column density; N_{MgII}/N_{FeII} increases from approximately unity ($\log U = -4$) to just over 100 at $\log U = -2$. Even though the first (7.646 eV, 7.870 eV) and second (15.035 eV, 16.18 eV) ionization potentials of Mg and Fe, respectively, are quite similar, the Fe is mainly in Fe^{+3} while the Mg is in Mg^{++} in our photoionization models, which we describe in the next section. This happens because it takes only 30.6 eV to ionize Fe^{++} to Fe^{+3} (and 54.8 eV to make Fe^{+4}) but 80 eV to remove another electron from Mg^{++} .

5. DISCUSSION

In this section we apply the idea of resonance scattering to the spatial extent of Mg II emission. We take as a model for the outflow a purely radial flow as illustrated in

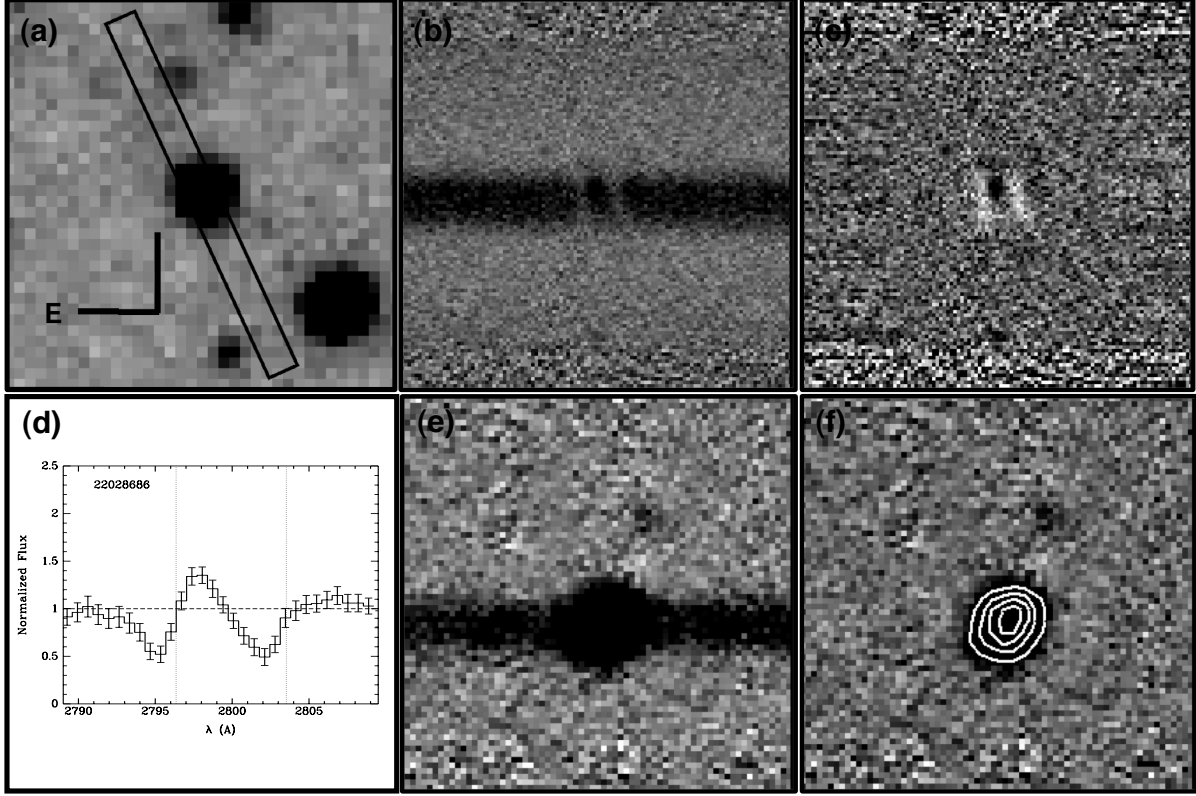


FIG. 9.— Observations of 22028686. (a) CFHT R-band image. The galaxy was observed with LRIS through a $1''.2$ by $15''.0$ slitlet at a position angle of 25.0° on mask msc22bb as described in Table 1 of Martin et al. (2012). (b) A 140 \AA wide segment of the blue LRIS spectrum centered on the Mg II doublet. Wavelength increases to the right, and northeast is up. The prominent absorption lines exhibit a velocity gradient across the galaxy; the centroid shifts blueward from the systemic velocity on the southwest side to approximately $-120 \pm 30 \text{ km s}^{-1}$ $1''.08$ (8.31 kpc) to the northeast. (c) Continuum subtracted blue spectrum. The Mg II emission component is spatially unresolved. The continuum emission subtends a larger angle than the resonance emission. (d) Integrated Mg II profile. The P-Cygni shape of the line profile, blueshifted absorption and redshifted emission, is typical of our Mg II emitter sample. (e) A 90 \AA wide segment of the red LRIS spectrum. The blended [O II] doublet is spatially extended. Wavelength increases to the right and northeast is up. Linearly spaced contours show a slight tilt of the nebular emission in the opposite sense of the velocity gradient apparent in panel (b). (f) Continuum subtracted red spectrum. The faint, serendipitous emission line near the northeastern end of the slit is $4''.44$ northeast of the peak continuum emission along the slit, and we identify it as [O II] emission from the $R = 24.8$ DEEP2 galaxy 22028464, which is visible $4''.66$ northeast of 22028686 in panel (a).

Figure 10. The radial component of the velocity is critical since the photons emitted by stars and H II regions emanate from smaller radii. Atoms in the circumgalactic medium (CGM) scatter photons at the resonance frequency in their rest frame. Outflowing gas absorbs photons blueward of resonance. The Doppler shift of the absorption trough directly reflects the velocity of the gas located between the galaxy and the observer. The redshifted emission from the far side of the outflow may escape and produce a redshifted emission line. The size of the scattering halo indicates the radius where the optical depth along a radial ray is approximately unity.

The clouds accelerate near the galaxy due to the radial decline in both thermal gas pressure and radiation pressure. The continuity equation gives the mass flux,

$$\dot{M}(r) = \Omega f_c \rho(r) v(r) r^2, \quad (1)$$

at radius r through the solid angle Ω subtended by the wind. The cloud covering fraction, f_c , describes the fraction of the outflow solid angle covered by low-ionization clouds (as seen from the galaxy).

Defining \bar{m}_{ion} as the mass in the warm outflow per ion, the column density between the observer and the launch

radius, R_0 , is

$$N_{ion} = \int_{R_0}^{\infty} \rho(r) / \bar{m}_{ion} dr. \quad (2)$$

Solving Eqn. 1 for $\rho(r)$, we see that the outflow density decreases with the inverse-square of the radius for the simple case of a constant velocity outflow with no mass-loading beyond the launch radius. For this example, the integral in Eqn. 2 yields a column density that declines inversely with the launch radius R_0 . Accurately measuring the ionic column density will still leave the mass-loss rate uncertain at the level of the plausible range of launch radii as well as the total mass per ion. Increases in column density strengthen the absorption trough significantly in the optically thin limit; but for saturated lines like the Mg II doublet, the range in gas velocity along the sightline largely determines the equivalent width of the intrinsic absorption troughs. The measured absorption equivalent width therefore provides only a lower limit on the ionic column density. The absorption troughs imprinted by outflows in galaxy spectra provide no constraint on the location of the gas along the sightline.

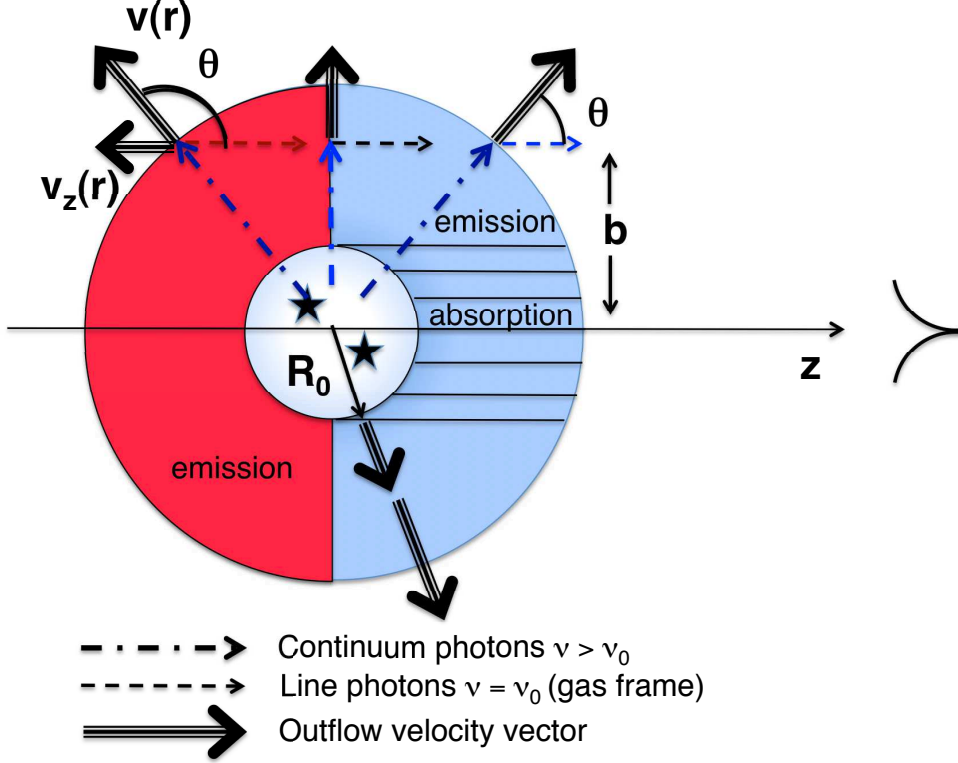


FIG. 10.— Schematic diagram of a spherical outflow around a galaxy illustrates an opening angle of $\Omega = 4\pi$ steradians, equivalent to a conical outflow with $\theta_{cone} = \pi$. The regions colored red and blue denote redshifted and blueshifted emission, respectively; and the hashed region denotes the location of atoms producing blueshifted absorption. For a delta-function line profile at the resonance ν_0 , atoms at each point along a sightline through the outflow absorb continuum photons at a unique frequency $\nu = \nu_0(1 + v(r)/c)^{-1}$, where $r = \sqrt{b^2 + z^2}$ along a sightline at impact parameter b . The emitted line photons have Doppler shifts corresponding to the range of projected outflow velocities, $v(r) \cos \theta$. For a constant velocity gradient, the density falls as r^{-3} , and we find the maximum Sobolev optical depth along the sightline at $z = 0$.

Resolving scattered line emission constrains the location and density of the gas flow. The scattering atoms must lie at radii at least as large as the projected impact parameter. The scattering optical depth scales with the gas density for a given model (or measurement) of the velocity gradient in the outflow.

In this section, we first we estimate the ionic density and radius at the scattering surface in 32016857 and TKRS 4389. Then we discuss the limits on the relationship between the total gas density and the ionic density. Finally, we illustrate the implications for the mass flux in low-ionization gas.

5.1. Density of Mg^+ in Outflowing Gas

We model the outflows with a radial velocity field. For 32016857, we picture a scenario where our slit intersects the outflow cone on only the west side of galaxy. In TKRS 4389, in contrast, the longslit observation resolves Mg II emission on both sides of the slit (Rubin et al. 2011). A simple model with a constant surface bright-

ness halo suggests the impact parameter of the scattering surface is $8.25 < b(\text{kpc}) < 13$ for TKRS 4389 (Rubin et al. 2011) and roughly 11.4 kpc from 32016857.

The interaction region where a resonance transition such as Mg II $\lambda 2796$ can be scattered depends on the line profile. To simplify the calculation, we consider a delta function line profile centered on the resonance frequency ν_0 (in the reference frame of the bulk flow). Photons emitted by the starburst at frequency ν propagate radially until they encounter a gas parcel with radial velocity $v(r_S) = c(\nu - \nu_0)/\nu_0$. We call the interaction spot the Sobolev point, r_S . Provided velocity v , μ , and the radial velocity gradient change slowly around r_S , the Sobolev expression (Sobolev & Gaposchkin 1960; Lamers & Cassinelli 1999) describes the scattering optical depth,

$$\tau_{\nu_0}^S = \frac{\pi e^2}{m_e c} f \lambda_0 n_i \left((1 - \mu^2) \frac{v(r)}{r} + \mu^2 \frac{dv}{dr} \right)^{-1}, \quad (3)$$

where f represents the transition oscillator strength.⁷

⁷ Note that the stimulated emission term has been dropped from

The incident photons and the velocity of the bulk flow are both radial, so the cosine of the angle θ between them takes the value $\mu = \cos \theta = 1$. The frequency of the photons absorbed from the starburst varies only with $v(r)$ for a spherical outflow.

With $\mu = 1$ in Eqn. 3, the Sobolev optical depth for the stronger Mg II transition is given by

$$\tau_{2796}^S(r) = 4.57 \times 10^{-7} \text{ cm}^3 \text{ s}^{-1} n_{\text{Mg}^+}(r_S) \left| \frac{dv}{dr} \right|_{r_S}^{-1}. \quad (4)$$

At some radius along the sightline at impact parameter $b \approx 11.4$ kpc, we expect the scattering optical depth for the starburst photons to be approximately unity. We estimate the gas density by setting $\tau_{2796}^S(r) \approx 1$ and obtain

$$n_{\text{Mg}^+} \approx 1.4 \times 10^{-9} \text{ cm}^{-3} \left| \frac{dv}{230 \text{ km s}^{-1} \frac{11.4 \text{ kpc}}{dr}} \right|_{r_S}. \quad (5)$$

If the sensitivity of our spectrum, rather than the radius of the last scattering surface, determines the observed extent of the scattered emission along the slit, then the optical depth (and the inferred density) would be higher than this estimate. However, we think modeling the spatial extent with the last scattering surface is roughly correct because the emission is not optically thick at $b \approx 11.4$ kpc; at the largest impact parameters where Mg II emission is detected, only $\lambda 2796$ is detected, consistent with a two-to-one flux ratio and an optical depth in $\lambda 2803$ less than unity. The gas density estimated from Eqn. 5 depends on the velocity gradient at the Sobolev point, and this radius is not uniquely determined from the impact parameter b alone.

Fig. 10 illustrates the geometry for the outgoing, scattered photons at impact parameter b . Along a sightline, the angle θ ranges from 90° where the flow is perpendicular to the sightline to a minimum, θ_{\min} , and maximum $\theta_{\max} \equiv 180^\circ - \theta_{\min}$, constrained by the Doppler shifts of the absorption and emission lines. The Doppler shift of a scattered photon reflects the projected velocity component, v_z , and will be most blueshifted (redshifted) as $\theta_{\min} \rightarrow 0^\circ$ ($\theta_{\max} \rightarrow 180^\circ$). These extrema mark the scattering that occurs at the largest radius along a sightline; and we infer the largest (smallest) radius from the lower (upper) limits on θ_{\min} . The error bars on the angle come from considering the projection of the radial velocity (measured in absorption) onto to the line-of-sight component measured at impact parameter b in emission. For 32016857, we estimate $38^\circ \leq \theta_{\min} \leq 75^\circ$, where the spectral fitting constrains the most blueshifted absorption ($(|V_{\text{Dop}}| + b)$) to the range $185 - 383 \text{ km s}^{-1}$; and the redshifted emission ($V_z + \sigma$) extends to at least $100 - 145 \text{ km s}^{-1}$. The maximum radius from which we detect scattered emission is therefore between $1.04b \approx 12 \text{ kpc}$ and $1.61b \approx 18 \text{ kpc}$.

We estimate an average velocity gradient of 230 km s^{-1} over 12 to 18 kpc. Substituting these values into Eqn. 5, we infer an ionic density between $8.9 \times 10^{-10} \text{ cm}^{-3}$ for $r_S = 18 \text{ kpc}$ ($\theta_{\min} = 38^\circ$) up to $1.3 \times 10^{-9} \text{ cm}^{-3}$ for $r_S = 12 \text{ kpc}$ ($\theta_{\min} = 75^\circ$). A specific form for the acceleration of the outflow, $v(r) = v_0 \sqrt{\ln r/R_0}$, demonstrates how a more physical model might change our density estimate. The

acceleration of a momentum driven outflow begins rapidly and then slows down with increasing distance. This model reaches a characteristic velocity v_0 at a radius a few times the launch radius, $r = 2.72R_0$. Choosing R_0 such that $v(r_S) = v_0$ and $r_S = 2.72R_0$, we obtain $dv/dr = 0.5v_0/r_S$. Placing the Sobolev point at $2.72R_0$ for comparative purposes, the estimated velocity gradient at r_S takes a value half as large as the constant acceleration limit; and our density estimate would increase by a factor of two.

For TKRS 4389, Rubin et al. (2011) measured the Doppler shift of the low-ionization absorption lines and fit a radius for the scattering halo to the surface brightness profile of the Mg II emission. Substituting their values of $V_{\text{Dop}} \approx 200 - 300 \text{ km s}^{-1}$ and $b \approx 8.25 - 12.4 \text{ kpc}$ into Eqn. 5, we estimate $n_{\text{Mg}^+} \approx 1.1 - 2.6 \times 10^{-9} \text{ cm}^{-3}$. Since the Sobolev radius could lie at radii as large as $r_S \approx 1.5b$, where we have used the Doppler shift of the $\lambda 2803$ emission, $v_z \approx 226 \text{ km s}^{-1}$ in Table 1 of Rubin et al. (2011), and $v = 300 \text{ km s}^{-1}$ to estimate $\theta_{\min} = \cos^{-1}(v_z(r_S)/v(r_S)) \approx 41^\circ$, we estimate a lower limit on the ionic density of roughly $0.73 \times 10^{-9} \text{ cm}^{-3}$. The slightly larger density, $n_{\text{Mg}^+} \approx 7 \times 10^{-9} \text{ cm}^{-3}$, found by Rubin et al. (2011) is consistent with substituting the -800 km s^{-1} Doppler shift of the blue wing on the Mg II profile into Eqn. 5 along with the minimum Sobolev radius. These arguments constrain the ionic density at the Sobolev radius in the TKRS 4389 outflow to the range $0.7 - 7 \times 10^{-9} \text{ cm}^{-3}$.

5.2. Gas Density

Given the ionic density n_{Mg^+} , the total gas density scales inversely with the ionization fraction, metallicity, and dust depletion. Defining the ionization fraction

$$\chi(\text{Mg}^+) \equiv n_{\text{Mg}^+}/n_{\text{Mg}}, \quad (6)$$

the hydrogen number density is

$$n_H = \frac{n_{\text{Mg}^+}}{\eta(\text{Mg})d(\text{Mg})\chi(\text{Mg}^+)}. \quad (7)$$

We scale to solar metallicity, $\eta(\text{Mg}) = 3.8 \times 10^{-5}$, which is appropriate (to a factor of two or better) for a wind loaded with interstellar gas from a galaxy with the stellar mass of the 32016857 (Zahid et al. 2011). We chose a fiducial value for the depletion of Mg onto grains typical of clouds in the Milky Way disk, $d(\text{Mg}) \approx 6.3 \times 10^{-2}$ (Savage & Sembach 1996), and note that a lower depletion similar to clouds in the Milky Way halo ($d \approx 0.28$) would lower our density estimate by a factor of four.

To estimate $\chi(\text{Mg}^+)$, we start with a rough assumption, which we relax later, namely that the bulk of the Mg ions are either Mg^+ or Mg^{++} . Then

$$\chi(\text{Mg}^+) \approx n_{\text{Mg}^+}/n_{\text{Mg}^{++}} = \frac{\alpha(\text{Mg}^+)}{c\sigma(\text{Mg}^+)} U^{-1}, \quad (8)$$

where the ionization parameter U is defined as

$$U \equiv \frac{Q}{4\pi r^2 c n_e}, \quad (9)$$

and

$$\epsilon_{\text{Mg}^+} \approx \frac{\alpha_{\text{Mg}^+}}{c\sigma_{\text{Mg}^+}} \approx 4.7 \times 10^{-4}. \quad (10)$$

In the last expression, the recombination rate $\alpha_{Mg^+}(T) \approx 3.5 \times 10^{-12} \text{ cm}^3 \text{ s}^{-1}$ at $T = 10^4 \text{ K}$ (Shull & van Steenberg 1982), and the photoionization cross section $\sigma_{Mg^+} \approx 2.5 \times 10^{-19} \text{ cm}^2$ (Verner et al. 1996). For 32016857, we estimate the ionizing photon luminosity $Q \approx 1.3 \times 10^{55} \text{ s}^{-1}$ from the $H\alpha$ luminosity (see description in Table 1) and the relationship in Kennicutt (1998).

Using Eqn. 8, we can solve for $n_H \approx n_e$

$$n_H \approx \left[\frac{n_{Mg^+} Q}{4\pi c \epsilon_{Mg^+} \eta(Mg^+), d(Mg) r^2} \right]^{1/2}. \quad (11)$$

At the location where $\tau_{2796} \approx 1$, the fiducial values give a H density

$$n_H = 0.30 \text{ cm}^{-3} \left(\frac{n_{Mg^+}}{10^{-9} \text{ cm}^{-3}} \right)^{1/2} \left(\frac{11.4 \text{ kpc}}{r_S} \right) \times \left(\frac{6.3 \times 10^{-2}}{d(Mg)} \right)^{1/2} \left(\frac{3.8 \times 10^{-5}}{\eta(Mg)} \right)^{1/2} \left(\frac{Q}{10^{55} \text{ s}^{-1}} \right)^{1/2} \quad (12)$$

The implied ionization parameter at the Sobolev point is

$$U(r_S) \approx 7.6 \times 10^{-2} \left(\frac{Q}{10^{55} \text{ s}^{-1}} \right) \left(\frac{0.30 \text{ cm}^{-3}}{n_e} \right) \times \left(\frac{11.4 \text{ kpc}}{r_S} \right)^2. \quad (13)$$

The resulting ionization fraction of Mg^+ ,

$$\chi(Mg^+) \approx 1.4 \times 10^{-3} \left(\frac{10^{55} \text{ s}^{-1}}{Q} \right) \left(\frac{n_e}{0.3 \text{ cm}^{-3}} \right) \times \left(\frac{r_S}{11.4 \text{ kpc}} \right)^2 \quad (14)$$

indicates most of the Mg in the warm phase of this outflow has been ionized to Mg^{++} . For comparison, inspection of Fig. 5 in Murray et al. (2007) shows that $\chi(Mg^+)$ lies between 0.1 and unity over broad range in gas density in ULIRG outflows due to the very low ionization parameter in dusty galaxies.

Using Cloudy version 13.00 (Ferland et al. 2013), we calculated the photoionization equilibrium of a constant density gas slab illuminated by a starburst and examined $\chi(Mg^+)$ as a function of U . Over the range $8 \times 10^{-4} < U < 0.08$, a simple power law fit gives

$$\chi(Mg^+) \approx n_{Mg^+}/n_{Mg} = \epsilon_{Mg^+} U^{-\alpha}, \quad (15)$$

with $\epsilon_{Mg^+} = 4 \times 10^{-4}$ and $\alpha = 0.94$. Dropping the assumption introduced in Eqn. 8, Equation 11 is modified to

$$n_H \approx \left[\frac{n_{Mg^+}}{\eta(Mg^+) d(Mg) \epsilon_{Mg^+}} \right]^{1/(1+\alpha)} \left[\frac{Q}{4\pi c r^2} \right]^{\alpha/(1+\alpha)} \quad (16)$$

For these improved values of $\chi(Mg^+)$ and α , Eqn. 12 becomes

$$n_H = 0.15 \text{ cm}^{-3} \left(\frac{n_{Mg^+}}{10^{-9} \text{ cm}^{-3}} \right)^{0.52} \left(\frac{11.4 \text{ kpc}}{r_S} \right)^{0.96} \times \left(\frac{6.3 \times 10^{-2}}{d(Mg)} \right)^{0.52} \left(\frac{3.8 \times 10^{-5}}{\eta(Mg)} \right)^{0.52} \left(\frac{Q}{10^{55} \text{ s}^{-1}} \right)^{0.48} \quad (17)$$

In the previous section, we argued that a sightline at impact parameter $b \approx 11.4 \text{ kpc}$ through the outflow includes emission from $r_S \approx b$ up to $r_S \approx 12 - 18 \text{ kpc}$. For this range of radii and $n_{Mg^+} = 1.4 \times 10^{-9} \text{ cm}^{-3}$, our best estimate for the hydrogen density at the Sobolev radius becomes

$$n_H \approx 0.12 - 0.18 \text{ cm}^{-3}. \quad (18)$$

To facilitate comparison to TKRS 4389, we have adopted the same fiducial corrections for abundance and depletion as Rubin et al. (2011). In contrast, however, application of our argument for the ionization correction to TKRS 4389 will yield a significantly larger H density than the Rubin et al. (2011) estimate of $n_H \approx 0.003 \text{ cm}^{-3}$ because they assumed $\chi(Mg^+) \approx 1$. Using the ionic density $n_{Mg^+} = 2.6 \times 10^{-9} \text{ cm}^{-3}$ (from the previous section) in Eqn. 12, we estimate $n_H = 0.28 - 0.67 \text{ cm}^{-3}$ for $r_S = 20 - 8 \text{ kpc}$. Over this same range of plausible values for r_S , our more accurate estimate from Eqn. 17 is $n_H = 0.15 - 0.33 \text{ cm}^{-3}$. We conclude that the gas density at the Sobolev points in the TKRS 4389 and 32016857 outflows are very similar.

5.3. Mass-Loss Rate

Using the H gas density from the previous section and assuming 1.4 atomic mass units per hydrogen atom, the mass loss rate in the warm gas from Eqn. 1 becomes

$$\dot{M}(r) = 500 \text{ M}_\odot \text{ yr}^{-1} \left(\frac{\Omega}{\pi} \right) \left(\frac{f_c}{1} \right) \left(\frac{r}{11.4 \text{ kpc}} \right)^2 \times \left(\frac{v}{230 \text{ km s}^{-1}} \right) \left(\frac{n_H}{0.3 \text{ cm}^{-3}} \right). \quad (19)$$

We have used the observation that resonance lines are blueshifted 100 km s^{-1} or more in 20% of star-forming galaxies at $z \sim 1$ (Martin et al. 2012), and the interpretation that the outflows must subtend roughly $0.2 \times 4\pi = 0.8\pi \approx \pi$ steradians on average. For 32016857, the mass flux in the (smooth) warm outflow is therefore approximately 330 - 500 $\text{M}_\odot \text{ yr}^{-1}$, which is 4 - 6 times larger than the SFR of 80 $\text{M}_\odot \text{ yr}^{-1}$ (for the Chabrier IMF). For TKRS 4389, we estimate a mass flux of 35 to 40 $\text{M}_\odot \text{ yr}^{-1}$.

We can use the empirical limits on the Mg II column density as a consistency check on the above argument. As can be seen in Figure 3, resonant emission fills in the Mg II absorption troughs, so the absorption equivalent width must be estimated from a fitted model. Even the weaker transition of the Mg II doublet is optically thick in any reasonable fit to the 32016857 spectrum; and, in Figure 3, it has an equivalent width of $W_{2803} = 2.04 \text{ \AA}$. We can use the linear relationship between W_{2803} and column density, valid in the optically thin limit, to place a lower limit on the ionic column density of $N(Mg^+) > 1.0 \times 10^{14} \text{ cm}^{-2}$.

Substituting Eqn. 1 into Equation 2 defines the relationship between this column density and the mass-loss rate. For a constant velocity outflow, $v(r) = V_{Dop}$, it yields

$$\dot{M} \approx \Omega \bar{m}_{ion} f_c^{-1} N_{ion} V_{Dop} R_0. \quad (20)$$

The mass-loss rate estimated from absorption lines therefore scales linearly with the inner radius of the outflow,

R_0 , which physically represents a launch radius. Using our mass-loss rate estimate from the scattered emission and the lower limit on the column density, however, we obtain an upper limit on the maximum launch radius

$$R_0 < 2.0 \text{ kpc} \left(\frac{\dot{M}}{500 \text{ M}_\odot \text{ yr}^{-1}} \right) \left(\frac{\pi}{\Omega} \right) \left(\frac{7 \times 10^{-16} \text{ g}}{\bar{m}} \right) \times \left(\frac{10^{14.5} \text{ cm}^{-2}}{N_{\text{Mg}^+}} \right) \left(\frac{230 \text{ km s}^{-1}}{V_{\text{Dop}}} \right). \quad (21)$$

Dynamical models of outflows relate the launch radius to the disk scaleheight (Mac Low et al. 1989; Murray et al. 2011), suggesting values of R_0 ranging from ≈ 100 pc for thin gas disks to several kiloparsecs for dwarf galaxies and very turbulent systems. We conclude that the strength of the saturated absorption lines, while in no way providing a test of our large ionization correction, are fully consistent with the ionic density of Mg^+ inferred from the scattered emission.

Up to this point, we have tacitly assumed a smooth outflow with $f_c \approx 1$. Higher resolution spectroscopy of outflows, however, indicates that saturated, low-ionization lines are not always black; and this partial covering of the continuum light indicates the warm outflows do not always have unity covering fraction (Martin & Bouché 2009). From a physical standpoint, interstellar gas is likely entrained in a hotter wind to create the outflow. In the Appendix to this paper, we outline simple physical arguments for the density and number of warm clouds in outflows. We find that the clumps have higher n_H than the smooth wind but reduce the overall mass-loss rate. The case of clouds confined by a hot wind produces higher gas densities in the outflow than do unconfined clumps. Both models suggest that clumps may lower the inferred mass-loss rate by up to a factor of 10. We conclude that the mass-loss rates in warm outflows from 32016857 and TKRS 4389 are at least $30\text{--}50 \text{ M}_\odot \text{ yr}^{-1}$ and $35\text{--}40 \text{ M}_\odot \text{ yr}^{-1}$, respectively. In this multi-phase model of the wind, we find the mass flux in the warm phase alone is comparable to the SFR.

6. IMPLICATIONS

One of the major goals of feedback studies is to measure the rate at which galactic winds remove gas from star-forming regions. Our empirical understanding of the relative mass flux originated with the study of starburst galaxies nearby enough to directly detect their winds in X-ray emission. The mass flux in both the $> 10^7 \text{ K}$ (Martin et al. 2002; Strickland & Heckman 2009) and 10^4 K (Lehnert & Heckman 1996; Martin 1999) phases of the winds was shown to be of order the SFR. At higher redshifts where winds presumably had an even larger impact on galaxy growth, the hot phase can rarely be directly observed; but unique observations of the warm-hot plasma now indicate it may contain 10 to 150 times more mass than the cold gas (Tripp et al. 2011).

In this paper we demonstrated how the resonance emission scattered by the warm gas in galactic winds can be used to measure the mass flux of low-ionization gas. Our discussion focused on the $z = 0.9392$ galaxy 32016857 because we detected Mg II emission that is significantly more extended than the nebular [O II] emission and marginally more extended than the near-UV continuum emission. This halo emission almost certainly results

from photon scattering because the Doppler shift of the Mg II emission is constant along the slit and does not share the prominent velocity gradient seen [O II] emission. The halo gas appears to be an outflow based on the P-Cygni line profile of Mg II in the integrated spectrum and the blueshift of the Fe II resonance absorption lines. This outflow must be collimated (i.e., an opening angle $\Omega < 4\pi$) because (1) the Mg II emission is only extended in one direction (to the east) along the slit and (2) the optical depths of the Mg II emission and absorption components differ, indicating departure from spherical symmetry.

Resolving the scattered emission improves our understanding of the mass-loss rate in the low-ionization phase of the outflow. In the Sobolev approximation, the ionic density and the radial velocity gradient determine the scattering optical depth along a sightline through the outflow. Based on the Doppler shift of the low-ionization (Fe II) absorption and the spatial extent of the Mg II emission in the 32016857 spectrum, we estimate an average velocity gradient of 230 km s^{-1} over 12 to 18 kpc for the outflow. Assuming we have detected the surface of unity scattering optical depth, an ansatz consistent with the doublet ratio of the Mg II emission, we directly calculate the density of Mg^+ ions, $n(\text{Mg II}) \approx (0.89 - 1.4) \times 10^{-9} \text{ cm}^{-3}$, in the outflow well beyond the star-forming region.

The implied mass flux depends on assumptions about metallicity, ionization fraction, depletion, and opening angle. We adopted a typical opening angle derived from the fraction of spectra of $z \sim 1$ star-forming galaxies showing blueshifted resonance absorption (Martin et al. 2012) and a metallicity that ensures consistency with the mass – metallicity relation at similar redshift (Zahid et al. 2011). The depletion of Mg onto grains is less constrained, but we argue that the likely values span only a factor of four based on the well-measured properties of Galactic clouds (Savage & Sembach 1996). The most uncertain parameter was the ionization correction, and we used photoionization modeling to show that the relation between the ionization fraction and the ionization parameter is nearly linear in the physical regime of interest. This calculation strongly suggests that most of the Mg in the outflow is Mg^{+2} and therefore not directly detected by our spectra. Following these physically plausible arguments, the mass flux in a smooth outflow is approximately $330 - 500 \text{ M}_\odot \text{ yr}^{-1}$ in 32016857, where the estimated uncertainty is a factor of four and the SFR $\approx 80 \text{ M}_\odot \text{ yr}^{-1}$. We reached very similar conclusions for TKRS 4389 outflow using analogous arguments.

Since we expect winds to be multi-phase, we further argued that the clumpiness of the warm gas must be taken into account to accurately characterize the systematic uncertainty in the mass-loss rate. In an Appendix, we demonstrated that smaller clouds result in higher densities and lower mass-loss rates (relative to the smooth outflow). The requirement that the clouds survive out to at least the observed distance of the scattering halo, however, places a physical limit on the minimum size of the clouds; and we show that outflow models with clouds reduce the inferred mass-loss rate by a factor of ten relative to the smooth wind model. Accounting for clouds lowers the inferred mass-loss rate in the warm outflow

but allows additional mass-loss in the hot phase. For 32016857 and TKRS 4389, we reach a reasonably robust conclusion that the outflow rates in the warm phase are at least comparable to the SFRs of the galaxies and could be an order of magnitude higher in the absence of a hot phase.

The mass loading factor, defined as $\eta \equiv \dot{M}/SFR$, serves a critical function in models of galaxy evolution. It scales inversely with the halo velocity dispersion, σ , for momentum-driven winds, but for energy-driven winds the relationship steepens to $\eta \propto \sigma^{-2}$. This slope affects how quickly the faint-end of the galaxy mass function flattens (Creasey et al. 2013; Puchwein & Springel 2013) as well as the slope of the mass-metallicity relation (Davé et al. 2012; Shen et al. 2012). To fit the galaxy mass function and mass – metallicity relation, the mass flux associated with a given star formation rate needs to increase as galaxy mass decreases. The typical normalization in numerical simulations sets the mass-loss rate to roughly the SFR at some fiducial mass. The relative mass fraction at widely different temperatures in these winds is not yet a robust theoretical prediction. Simulations focusing on the winds rather than cosmological structure have just begun to include pressure from radiation and cosmic rays which analytic calculations suggest are important (Murray et al. 2005, 2011; Breitschwerdt et al. 1991; Everett et al. 2008; Socrates et al. 2008). At least in one recent simulation, Hopkins et al. (2012) find that the warm, $2000 < T(K) < 10^5$, phase dominates the mass transport in outflows from SMC-like dwarf galaxies and remains comparable to the mass flux in the hot wind in a model chosen to match the properties of a high-redshift starburst.

At this time, TKRS 4389 (Rubin et al. 2011) and 32016857 remain the only clear examples of Mg II scattered by outflows. Among 145 LRIS spectra of $0.4 < z < 1.4$ galaxies, including 22 with very prominent Mg II emission, we found only three examples of spatially resolved Mg II emission. Unlike 32016857, the line emission resolved around 32010773 and 12019973 is not necessarily scattered; it could come directly from H II regions as it is no more extended than the nebular [O II] emission and not clearly distinct kinematically. We suggest, in spite of the large number of null detections, that diffuse Mg II emitting halos may be a common property of star-forming galaxies at intermediate redshifts. Approximately 15% of our sample have prominent Mg II emission (Kornei et al. 2013). A larger fraction of the spectra show blueshifted resonance absorption lines indicative of outflowing gas (Martin et al. 2012). The resonance emission scattered by these outflows could be attenuated by the LRIS slit or destroyed by dust absorption, a scenario supported by the observed tendency for Mg II emitters to have bluer than average $U - B$ color (Martin et al. 2012; Kornei et al. 2013). Based on the properties of TKRS 4389 and 32016857 – namely their high sSFRs and unusually high B-band luminosities for their $U - B$ colors, we suggest that the scattered emission is brighter around these galaxies than it is near more typical Mg II emitters.

While much of their halo emission may simply lie below current detection limits, intermediate redshift galaxies may prove an ideal environment for pinning down mass-

loss rates. Outflows were more common at $z \sim 1$ than today due to the higher cosmic SFR (Hopkins & Beacom 2006) and smaller galaxy sizes (Simard et al. 1999; Lilly et al. 1998). Most of the star-forming galaxies have developed well-defined disks by this time. The orientation of these galactic disks relative to halo sightlines probed by background quasars (or galaxies) provides a valuable means to distinguish intervening absorption created by outflows from other sources such as infalling gas (Bordoloi et al. 2011). The relative metallicity of the galactic disk and halo clouds have also been used to identify accreting gas (Ribaudo et al. 2011). Scattered emission from an outflow becomes easier to detect as the physical area subtended by a fixed spectroscopic aperture increases, and the angular diameter distance increases with redshift out to $z \approx 1.6$. Since cosmic expansion reduces the observed surface brightness emission as $(1+z)^{-4}$, the brightest scattered halo emission may be found at redshifts somewhat less than the maximum angular diameter distance. In the future, mapping the Mg II line emission scattered by circumgalactic gas should, in principle, provide a means to directly measure η in galaxies over a broad mass range. The results from the first two detections of scattered Mg II emission strongly suggest very substantial mass-loss in the outflows from intermediate redshift galaxies.

We thank the the DEEP2 and AEGIS teams for providing ancillary data on galaxy properties, Mike Shull for stimulating discussions, and the referee for thoughtful comments on the manuscript. This research was supported by the National Science Foundation under AST-1109288 (CLM), the David & Lucile Packard Foundation (AES and CLM), the Alfred P. Sloan Foundation and NSF CAREER award AST-1055081 (ALC), a Dissertation Year Fellowship at UCLA (KAK), and an NSF Graduate Research Fellowship Program (AP). The research was partially carried out at the Aspen Center for Physics which is supported by the National Science Foundation under Grant No. NSF PHY05-51164. We also wish to recognize and acknowledge the highly significant cultural role that the summit of Mauna Kea has always had within the indigenous Hawaiian community. It is a privilege to be given the opportunity to conduct observations from this mountain.

Facilities: Keck

TABLE 1
GALAXY PROPERTIES

| Property | 32016857 |
|---|----------------------|
| RA | 23:29:24.954 |
| DEC | +00:07:05.85 |
| Redshift ^a | 0.939196 |
| B (AB mag) | 22.49 |
| $M_B - 5 \log h_{70}$ (AB mag) ^b | -21.59 |
| $U - B$ ^b | 0.44 |
| $\log M_*/M_\odot$ ^c | 9.82 |
| V_1 (km s ⁻¹) ^a | -91 ± 15 |
| V_{Dop} (km s ⁻¹) ^a | -227 ± 82 |
| $\log[N_{Dop}(Fe^+)C_f]$ (cm ⁻²) ^a | 14.41 - 15.53 |
| SFR (M _⊙ yr ⁻¹) ^d | 78 |
| sSFR (yr ⁻¹) | 1.2×10^{-8} |

^aFrom Martin et al. (2012).

^bFrom Willmer et al. (2006).

^cFrom Bundy et al. (2006).

^dAfter scaling the flux of the red LRIS spectrum to match the DEEP2 magnitude of $I_{AB} = 21.70$, we measured an integrated [O II] line flux of 6.25×10^{-16} ergs s⁻¹ cm⁻², corresponding to an uncorrected (for extinction) line luminosity of 2.79×10^{42} erg s⁻¹. To estimate the SFR, we use the average ratio of [O II] to H α luminosity (0.40) measured by Moustakas et al. (2006) among nearby galaxies with $M_B \approx -21.6$. By adopting the mean ratio for galaxies with luminosities similar to 32016857, this calibration takes the strong correlation between line ratio and reddening into account. Finally, dividing the SFR obtained from the (Kennicutt 1998) H α calibration by 1.78, we obtain a SFR of $78 M_\odot \text{ yr}^{-1}$ for a Chabrier IMF from 0.1 to $100 M_\odot$.

TABLE 2
SPECTRAL LINE MEASUREMENTS

| Transition | λ_0 (Å) | $W_r(\lambda)$ (Å) |
|---------------------|---------------------------|-----------------------|
| Fe II* | 2365.56 | -0.47 ± 0.34 |
| Fe II* | 2381.49 | ... |
| Fe II* | 2396.26 | -0.78 ± 0.32 |
| Fe II* | 2612.65 | 0.31 ± 0.33 |
| Fe II* | 2626.45 | -1.41 ± 0.32 |
| Fe II* | 2632.77 | -0.32 ± 0.24 |
| Fe II | 2260.21 | < 0.6 |
| Fe II | 2344.21 | 1.41 ± 0.22 |
| Fe II | 2374.46 | 0.88 ± 0.19 |
| Fe II | 2382.77 | 0.99 ± 0.18 |
| Fe II | 2586.65 | 1.84 ± 0.22 |
| Fe II | 2600.17 | 2.07 ± 0.24 |
| Mg II | 2796.35 | 0.34 ± 0.39 |
| Mg II | " | -2.13 ± 0.29^b |
| Mg II | 2803.53 | 0.85 ± 0.22 |
| Mg II | " | -1.16 ± 0.27^b |
| CIII] | 1908.73 | -1.57 ± 0.47 |
| CII] | 2326 ^a | -2.06 ± 0.37 |
| [Ne V] | 3426.98 | < 0.84 |
| [O II] | 3727.09, 3729.88 | -128.2 ± 3.1 |
| [Ne III], He I | 3869.85, 3868.63 | -14.16 ± 0.95 |
| H8, He I | 3890.15, 3889.75 | -6.83 ± 0.63 |
| H I, [Ne III], He I | 3971.19, 3968.58, 3965.85 | -8.73 ± 1.03 |
| H δ | 4102.90 | -9.55 ± 0.70 |
| H γ | 4341.69 | -16.68 ± 1.36 |

^aBlend of $\lambda 2324.22$, $\lambda 2325.41$, $\lambda 2327.65$, $\lambda 2328.84$

^bIn the integrated spectrum, the observed flux in Mg II emission is $F(\lambda 2796) \approx 1.5 \times 10^{-17}$ ergs s⁻¹ cm⁻² and is $F(\lambda 2803) \approx 1.0 \times 10^{-17}$ ergs s⁻¹ cm⁻² to roughly 20% accuracy.

APPENDIX

A. MASS-LOSS RATE FOR A CLUMPY WIND

The scattering optical depth of the $\lambda 2796$ line is

$$\tau_{2796} = n_{\text{MgII}} \sigma_{2796}(\Delta v) l. \quad (\text{A1})$$

The cross-section of the $\lambda 2796$ transition, with units of cm^2 , is

$$\sigma_{2796}(\Delta v) = \frac{\pi e^2}{m_e c} f \frac{\lambda_0}{\Delta v}, \quad (\text{A2})$$

where λ_0 is the wavelength of the transition, e and m_e are the charge and mass of an electron, and $f = 0.62$ is the oscillator strength of the transition. The quantity Δv is the velocity range over which the ions are distributed; for example, where the gas exhibits only thermal motions, $\Delta v = v_{\text{th}}$, so that the velocity spread is simply the thermal velocity spread. The velocity spread may be much larger than v_{th} if the gas exhibits bulk motions.

In fact the expression (A1) for the optical depth depends on two unknown quantities, a characteristic length scale l associated with the outflow, and Δv . We scale Δv to the ion thermal velocity $v_{\text{th}} \approx 2(T/10^4 \text{ K})^{1/2} \text{ km s}^{-1}$ of a Mg^+ ion, and introduce

$$\sigma_{2796}^{\text{th}} = \frac{\pi e^2}{m_e c} f \frac{\lambda_0}{v_{\text{th}}} \approx 2.6 \times 10^{-12} \left(\frac{T}{10^4 \text{ K}} \right)^{-1/2} \text{ cm}^2. \quad (\text{A3})$$

Using these, eqn. (A1) becomes

$$\tau_{2796} = n_{\text{MgII}} \sigma_{2796}^{\text{th}} \frac{v_{\text{th}}}{\Delta v} l = n_{\text{MgII}} \sigma_{2796}^{\text{th}} l_{\text{eff}}, \quad (\text{A4})$$

where we have introduced the effective scattering length

$$l_{\text{eff}} \equiv \frac{v_{\text{th}}}{\Delta v} l. \quad (\text{A5})$$

Specifying a physical model for the outflowing gas determines l_{eff} . We will scale to a smooth wind model, in which the effective scattering length is the Sobolev length

$$l_{\text{Sob}} \equiv \frac{v_{\text{th}}}{dv/dr}, \quad (\text{A6})$$

where $dv/dr \approx v(r)/r_S$ is the velocity gradient in the wind at the point where $\tau_{2796} = 1$.

For our galaxy, taking the largest radius at impact parameter b where scattered emission is detected,

$$l_{\text{Sob}} \approx \left(\frac{v_{\text{th}}}{v} \right) \approx 90 \text{ pc} \left(\frac{v_{\text{th}}}{2 \text{ km s}^{-1}} \right) \left(\frac{280 \text{ km s}^{-1}}{v} \right) \left(\frac{r_S}{12 \text{ kpc}} \right). \quad (\text{A7})$$

A.1. Physical wind models

We consider three models for the outflow, a smooth $T \approx 10^4 \text{ K}$ wind, an outflow consisting of unconfined $T \approx 10^4 \text{ K}$ clouds or clumps, and a two-phase hot ($T_h \approx 10^8 \text{ K}$ and smooth) together with a cold ($T \approx 10^4 \text{ K}$) and clumpy outflow, in which the cold clouds are confined by thermal pressure of the hot gas. The hot gas in the last model is naturally provided by supernovae exploding in the galaxy, at a rate proportional to the star formation rate (about one supernova per century for a star formation rate of one solar mass per year).

A.1.1. The smooth wind model

In a smooth wind the characteristic velocity spread is $\Delta v = v_{\text{th}}$ and the characteristic length l is the Sobolev length

$$l_{\text{eff}} = l_{\text{Sob}} \equiv \frac{v_{\text{th}}}{dv/dr}. \quad (\text{A8})$$

The logarithmic derivative of the wind velocity

$$\Gamma(r) \equiv \frac{r}{v} \frac{dv}{dr} \quad (\text{A9})$$

is of order unity in the wind acceleration region, so

$$l_{\text{Sob}} = \Gamma^{-1} \left(\frac{v_{\text{th}}}{v} \right) r \ll r. \quad (\text{A10})$$

A.1.2. Unconfined clouds

Our second model assumes that the outflow consists of a large number of unconfined clouds. If the clouds are unconfined, e.g., if their gas pressure exceeds that of any hot outflow, then their size along the direction of acceleration \mathbf{g} is

$$l = \frac{c_s^2}{g} \approx \left(\frac{c_s}{v_c} \right)^2 r \approx 100 \text{ pc}, \quad (\text{A11})$$

where $c_s \approx 10 \text{ km s}^{-1}$ is the sound speed of the $T \approx 10^4 \text{ K}$ gas in the clouds, and v_c is the circular velocity of the host galaxy, which is of order the outflow velocity. The effective size of the cloud is

$$l_{eff} = \left(\frac{c_s}{\Delta v} \right) \left(\frac{c_s}{v} \right) \left(\frac{v_{th}}{v} \right) r, \quad (\text{A12})$$

where we approximate $v_c \approx v$, the outflow velocity.

The velocity spread $\Delta v \approx v_{th}$ if there are no bulk flows in the clouds, in which case $l_{eff} = l_{Sob}$. In the more likely case that there are transverse bulk flows (expansions, in particular), then Δv , could be of order c_s . In that case,

$$l_{eff} \approx \frac{c_s}{v} l_{Sob} \approx 0.1 l_{Sob}. \quad (\text{A13})$$

A.1.3. Confined clouds

Our third model assumes that the cold gas consists of clouds confined by hot gas. With a star formation rate of $\sim 80 M_\odot \text{ yr}^{-1}$, and an expected supernova rate of nearly one per year, it is likely that the galaxy possesses a hot ($T_h \sim 10^8 \text{ K}$) gas component. Since the sound speed of this hot gas exceeds the circular velocity of the galaxy by a large amount, it will flow out with a bulk velocity of a few times its sound speed, $c_h \approx 1000 \text{ km s}^{-1}$. This gas will act to pressurize the cold gas clouds, to accelerate them, and to disrupt them.

A priori, the cold clouds could have any size l_{cl} and a range of internal velocities Δv . However, we argue that there is a well defined lower limit to l_{cl} , as follows.

Both simulations (Klein et al. 1994) and experiments (Hansen et al. 2007) demonstrate that cold clouds embedded in such hot outflows are destroyed on a few tens of cloud crushing times. The cloud crushing time is defined as (Klein et al. 1994)

$$\tau_{cc} \equiv \left(\frac{n_c}{n_h} \right)^{1/2} \frac{l_{cl}}{v_s}, \quad (\text{A14})$$

where $n_c = n_H^{\tau=1}$ and n_h are the number densities of the cold and hot gas, and $v_s \approx v_h$ is the velocity of the shock in the hot flow.

The clouds must live long enough to reach $R_{\tau=1} \approx 11.4 \text{ kpc}$, which allows us to set a lower limit to l_{cl} :

$$30 \tau_{cc} \gtrsim \left(\frac{R_{\tau=1}}{v} \right), \quad (\text{A15})$$

leading to a cloud length

$$l_{cl} \gtrsim \left(\frac{v_h}{30v} \right)^{4/3} \left(\frac{n_h}{n_H^{\tau=1}(\text{Sob})} \right)^{2/3} \left(\frac{r}{l_{\text{Sob}}} \right)^{4/3} \left(\frac{v_{th}}{\Delta v} \right)^{1/3} l_{\text{Sob}}. \quad (\text{A16})$$

We have scaled the clouds survival time to 30 cloud crushing times. Scaling to a hot wind with a mass loss rate similar to the star formation rate, and assuming that $\Delta v \sim v_{line}$,

$$l_{cl} \approx 170 \left(\frac{R}{11.4 \text{ kpc}} \right) \left(\frac{n_h}{2 \times 10^{-3} \text{ cm}^{-3}} \right)^{1/2} \text{ pc}. \quad (\text{A17})$$

As with the unconfined cloud model, this length is similar to the Sobolev length associated with a smooth wind. The characteristic velocity spread $\Delta v \sim v_{line}$; it cannot be larger than the observed linewidth. Then

$$l_{eff} \equiv \left(\frac{v_{th}}{v} \right) l_{cl} \approx 1.7 \text{ pc}. \quad (\text{A18})$$

If the gas being removed from the cloud is over-ionized (so that all the MgII ions are removed) before it is accelerated, Δv could be as small as v_{th} , but as we will see this would lead to a large mass loss rate in the cold component.

A.2. Mass-loss rates

For a smooth outflow, the continuity equation

$$\dot{M}_w = \Omega f_c \bar{m} r^2 n_H v \quad (\text{A19})$$

gives Eqn. 12. Note that η_{Mg} , d_{Mg} , and ϵ_{Mg^+} all enter to the one half power, so that the estimate for the mass loss rate is only moderately sensitive to these quantities. Observations indicate, however, that the warm outflows are clumpy (Martin & Bouché 2009; Bordoloi et al. 2012). Taking $f_c \approx 1$, where f_c describes the fraction of the outflow cone

covered by clouds as seen from the galaxy, places an upper limit to the mass loss rate in warm (10^4 K) gas for a fixed density, $\bar{m}n_H$.

For illustration, we consider a bi-conical outflow of half-opening angle θ_{bc} such that the outflow subtends a solid angle $\Omega = \Omega_{bc} \equiv 2\pi \int_0^{\theta_{bc}} \sin \theta d\theta$. In light of the limited observational constraints on the orientation of the outflows in 32016857 and TKRS 4389, the symmetry axis of the cone can be taken perpendicular to the observer's sightline to illustrate the impact of clumpiness on the density and mass-loss rate.

A.2.1. Clumpy outflows

The mass of a single cloud is

$$m_{cl} = \frac{4\pi}{3} l_{cl}^3 \bar{m} n_{H,cl}. \quad (\text{A20})$$

Over the velocity width of the emission line, Δv_{el} , clouds at the projected radius where $\tau_{2796}(b) \approx 1$ have to reflect a large fraction of the continuum. To find the number of clouds at this impact parameter which have projected velocities consistent with the linewidth, consider an annulus of width Δb on the sky. Over the velocity width of a single cloud, Δv_{cl} , the clouds must cover a projected area $2\theta b \Delta b$. In addition, the clouds have to cover the range of velocity seen in the emission line. Together these two constraints give a lower limit to the number of clumps or clouds given by

$$N_{cl} = 2f_v \left(\frac{\theta_{bc}}{\pi} \right) \left(\frac{\Delta v_{el}}{\Delta v_{cl}} \right) \left(\frac{b}{l_{cl}} \right) \left(\frac{\Delta b}{l_{cl}} \right), \quad (\text{A21})$$

where f_v is the fraction of the linewidth covered by clouds. The total mass in clouds is $M_{cl} = N_{cl} m_{cl}$, or

$$M_{cl} = 2 \left(\frac{\theta_{bc}}{\pi} \right) f_v \left(\frac{\Delta v_{el}}{\Delta v_{cl}} \right) \left(\frac{b}{l_{cl}} \right) \left(\frac{\Delta b}{l_{cl}} \right) \cdot \frac{4\pi}{3} l_{cl}^3 \bar{m} n_{H,cl}. \quad (\text{A22})$$

The mass loss rate is calculated using the crossing time,

$$\tau_{\text{cross}} = \frac{\Delta b}{v_x(b)} = \frac{\Delta b}{v \sin \theta} = \frac{\Delta b}{v} \cdot \frac{r}{b}. \quad (\text{A23})$$

We find

$$\dot{M}_{cl} = \bar{m} r^2 v \cdot 4\theta_{bc} f_v n_{H,cl} \cdot \frac{2}{3} \cdot \left(\frac{l_{cl}}{r} \right) \left(\frac{b}{r} \right)^2 \left(\frac{\Delta v_{el}}{\Delta v_{cl}} \right). \quad (\text{A24})$$

Using equation (A19), we scale the mass-loss rate in the clumpy outflow to the that of the smooth outflow,

$$\dot{M}_{cl} = \left(\frac{4\theta_{bc}}{\Omega_{bc}} \right) \left(\frac{f_v}{f_c} \right) \cdot \left(\frac{n_{H,cl}}{n_H} \right) \cdot \left(\frac{2}{3} \right) \left(\frac{l_c}{r} \right) \left(\frac{b}{r} \right)^2 \left(\frac{\Delta v_{el}}{\Delta v_{cl}} \right) \dot{M}_w. \quad (\text{A25})$$

It is convenient to scale the cloud density to a smooth wind:

$$n_{H,cl} = n_H(\text{Sob}) \left(\frac{l_{\text{Sob}}}{l_{eff}} \right)^{1/2}, \quad (\text{A26})$$

where

$$n_H(\text{Sob}) \equiv \left[\frac{n_\gamma n_{\text{MgII}}^{\tau=1}(\text{Sob})}{\eta_{Mg} d_{Mg} \epsilon_{\text{Mg}^+}} \right]^{1/2}. \quad (\text{A27})$$

For a clumpy outflow, the effective length scale for absorption over the linewidth contributed by a single clump is simply related to the properties of a cloud,

$$l_{eff} \approx \left(\frac{v_{th}}{\Delta v} \right) l_{cl}. \quad (\text{A28})$$

The density of a clump or cloud in the wind will exceed that of the smooth wind by a factor

$$n_{H,cl} = n_H \left(\frac{l_{\text{Sob}}}{l_{cl}} \right)^{1/2} \left(\frac{\Delta v_{cl}}{v_{th}} \right)^{1/2}. \quad (\text{A29})$$

A.2.2. Comparison of Clumpy and Smooth Outflows

Using equations (A25) and (A29),

$$\dot{M}_{cl} = \frac{2}{3} \left(\frac{4\theta_{bc}}{\Omega_{bc}} \right) \left(\frac{f_v}{f_c} \right) \left(\frac{l_{\text{Sob}}}{r} \right) \left(\frac{l_{cl}}{l_{\text{Sob}}} \right)^{1/2} \left(\frac{b}{r} \right)^2 \cdot \left(\frac{\Delta v_{el}}{\Delta v_{cl}} \right)^{1/2} \left(\frac{\Delta v_{cl}}{v_{th}} \right)^{1/2} \dot{M}_w. \quad (\text{A30})$$

The square-root dependence of the mass loss rate on the cloud size l_{cl} indicates this estimate is fairly robust. To illustrate how the clouds affect the mass-loss estimate, we take $r = (1.0 - 1.5)b \approx b$, $4\theta_{bc}/\Omega_{bc} \approx 1$, and $f_v/f_c \approx 1$.

For an unconfined clumpy outflow, with $l_{cl} \approx 0.1 l_{Sob}$ and $\Delta v \approx c_s$, the mass loss rate

$$\dot{M}_{cl} \approx 0.10 \left(\frac{\Delta v_{el}}{280} \right) \left(\frac{10}{\Delta v_{cl}} \right)^{1/2} \left(\frac{2}{\Delta v_{th}} \right)^{1/2} \left(\frac{l_{Sob}}{90} \right)^{1/2} \left(\frac{l_{cl}}{9} \right)^{1/2} \left(\frac{12}{r} \right) \dot{M}_w \quad (A31)$$

is about one tenth the smooth wind rate. The mass-loss is also lower when we assume hot gas confines the clouds. For a confined clumpy wind, with $l_{cl} \approx l_{Sob}$ but $\Delta v \approx v_{line}$, the mass loss rate is

$$\dot{M}_{cl} \approx 0.06 \left(\frac{\Delta v_{el}}{280} \right) \left(\frac{280}{\Delta v_{cl}} \right)^{1/2} \left(\frac{2}{\Delta v_{th}} \right)^{1/2} \left(\frac{l_{Sob}}{90} \right)^{1/2} \left(\frac{l_{cl}}{90} \right)^{1/2} \left(\frac{12}{r} \right) \dot{M}_w. \quad (A32)$$

Allowing for very small cloud sizes l_{cl} , as might be the case in a hot-gas confined clumpy outflow, indicates that the mass loss rate can up to a factor of approximately 10 times lower than that estimated under the smooth outflow assumption.

Whether small clouds can survive the acceleration process remains open to some debate. The fiducial values of 9 and 90 pc used here lie at the low end of the size ranges recently estimated from photoionization modeling of circumgalactic gas clouds in both nearby galaxies (Stocke et al. 2013) and intermediate redshift absorption-line systems (Meiring et al. 2013). These calculations offer a physical argument nonetheless for the maximum amount by which the smooth outflow model may overestimate the mass-loss rate. They suggest that the mass-loss rate in the warm outflow could be just 10% of the smooth wind mass-loss rate. If such clouds are present in the wind, then the hot wind will of course contribute additional mass flux.

REFERENCES

- Behroozi, P. S., Conroy, C., & Wechsler, R. H. 2010, *ApJ*, 717, 379
 Bordoloi, R., Lilly, S. J., Kacprzak, G. G., & Churchill, C. W. 2012, *ArXiv e-prints*
 Bordoloi, R., et al. 2011, *ApJ*, 743, 10
 Bouché, N., Hohensee, W., Vargas, R., Kacprzak, G. G., Martin, C. L., Cooke, J., & Churchill, C. W. 2012, *MNRAS*, 426, 801
 Bouché, N., et al. 2010, *ApJ*, 718, 1001
 Breitschwerdt, D., McKenzie, J. F., & Voelk, H. J. 1991, *A&A*, 245, 79
 Bundy, K., et al. 2006, *ApJ*, 651, 120
 Chabrier, G. 2003, *PASP*, 115, 763
 Chen, Y.-M., Tremonti, C. A., Heckman, T. M., Kauffmann, G., Weiner, B. J., Brinchmann, J., & Wang, J. 2010, *AJ*, 140, 445
 Coil, A. L., Newman, J. A., Kaiser, N., Davis, M., Ma, C.-P., Kocevski, D. D., & Koo, D. C. 2004, *ApJ*, 617, 765
 Coil, A. L., Weiner, B. J., Holz, D. E., Cooper, M. C., Yan, R., & Aird, J. 2011, *ApJ*, 743, 46
 Coil, A. L., et al. 2008, *ApJ*, 672, 153
 Creasey, P., Theuns, T., & Bower, R. G. 2013, *MNRAS*, 437
 Davé, R., Finlator, K., & Oppenheimer, B. D. 2012, *MNRAS*, 421, 98
 Dekel, A., & Birnboim, Y. 2006, *MNRAS*, 368, 2
 Dekel, A., et al. 2009, *Nature*, 457, 451
 Erb, D. K., Quider, A. M., Henry, A. L., & Martin, C. L. 2012, *ApJ*, 759, 26
 Everett, J. E., Zweibel, E. G., Benjamin, R. A., McCammon, D., Rocks, L., & Gallagher, III, J. S. 2008, *ApJ*, 674, 258
 Ferland, G. J., et al. 2013, *RevMexAA*, 49, 137
 Giallisco, M., et al. 2011, *ApJ*, 743, 95
 Hansen, J. F., Robey, H. F., Klein, R. I., & Miles, A. R. 2007, *ApJ*, 662, 379
 Heckman, T. M. 2003, in *Revista Mexicana de Astronomia y Astrofisica Conference Series*, Vol. 17, *Revista Mexicana de Astronomia y Astrofisica Conference Series*, ed. V. Avila-Reese, C. Firmani, C. S. Frenk, & C. Allen
 Heckman, T. M., et al. 2011, *ApJ*, 730, 5
 Hopkins, A. M., & Beacom, J. F. 2006, *ApJ*, 651, 142
 Hopkins, P. F., Keres, D., Murray, N., Hernquist, L., Narayanan, D., & Hayward, C. C. 2013, *ArXiv e-prints*
 Hopkins, P. F., Quataert, E., & Murray, N. 2012, *MNRAS*, 421, 3522
 Kacprzak, G. G., Churchill, C. W., & Nielsen, N. M. 2012, *ApJ*, 760, L7
 Kennicutt, Jr., R. C. 1998, *ARA&A*, 36, 189
 Kereš, D., Katz, N., Fardal, M., Davé, R., & Weinberg, D. H. 2009, *MNRAS*, 395, 160
 Kereš, D., Katz, N., Weinberg, D. H., & Davé, R. 2005, *MNRAS*, 363, 2
 Klein, R. I., McKee, C. F., & Colella, P. 1994, *ApJ*, 420, 213
 Kornei, K. A., Shapley, A. E., Erb, D. K., Steidel, C. C., Reddy, N. A., Pettini, M., & Bogosavljević, M. 2010, *ApJ*, 711, 693
 Kornei, K. A., Shapley, A. E., Martin, C. L., Coil, A. L., Lotz, J. M., Schiminovich, D., Bundy, K., & Noeske, K. G. 2012, *ApJ*, 758, 135
 Kornei, K. A., Shapley, A. E., Martin, C. L., Coil, A. L., Lotz, J. M., & Weiner, B. J. 2013, *ArXiv e-prints*
 Lamers, H. J. G. L. M., & Cassinelli, J. P. 1999, *Introduction to Stellar Winds* (Cambridge, UK: Cambridge University Press, June 1999.)
 Law, D. R., Steidel, C. C., Shapley, A. E., Nagy, S. R., Reddy, N. A., & Erb, D. K. 2012, *ApJ*, 759, 29
 Lehnert, M. D., & Heckman, T. M. 1996, *ApJ*, 462, 651
 Lilly, S., et al. 1998, *ApJ*, 500, 75
 Mac Low, M.-M., McCray, R., & Norman, M. L. 1989, *ApJ*, 337, 141
 Martin, C. L. 1999, *ApJ*, 513, 156
 —. 2005, *ApJ*, 621, 227
 —. 2006, *ApJ*, 647, 222
 Martin, C. L., & Bouché, N. 2009, *ApJ*, 703, 1394
 Martin, C. L., Kobulnicky, H. A., & Heckman, T. M. 2002, *ApJ*, 574, 663
 Martin, C. L., Shapley, A. E., Coil, A. L., Kornei, K. A., Bundy, K., Weiner, B. J., Noeske, K. G., & Schiminovich, D. 2012, *ApJ*, 760, 127
 Meiring, J. D., Tripp, T. M., Werk, J. K., Howk, J. C., Jenkins, E. B., Prochaska, J. X., Lehner, N., & Sembach, K. R. 2013, *ApJ*, 767, 49
 Morton, D. C. 2003, *ApJS*, 149, 205
 Moustakas, J., Kennicutt, Jr., R. C., & Tremonti, C. A. 2006, *ApJ*, 642, 775
 Murray, N., Martin, C. L., Quataert, E., & Thompson, T. A. 2007, *ApJ*, 660, 211
 Murray, N., Ménard, B., & Thompson, T. A. 2011, *ApJ*, 735, 66
 Murray, N., Quataert, E., & Thompson, T. A. 2005, *ApJ*, 618, 569
 Newman, J. A., et al. 2012, *ArXiv e-prints*
 Pettini, M., Rix, S. A., Steidel, C. C., Adelberger, K. L., Hunt, M. P., & Shapley, A. E. 2002, *ApJ*, 569, 742
 Phillips, A. C. 1993, *AJ*, 105, 486
 Prochaska, J. X., Kasen, D., & Rubin, K. 2011, *ApJ*, 734, 24
 Puchwein, E., & Springel, V. 2013, *MNRAS*, 428, 2966
 Ribado, J., Lehner, N., Howk, J. C., Werk, J. K., Tripp, T. M., Prochaska, J. X., Meiring, J. D., & Tumlinson, J. 2011, *ApJ*, 743, 207
 Rubin, K. H. R., Prochaska, J. X., Koo, D. C., Phillips, A. C., & Weiner, B. J. 2010, *ApJ*, 712, 574
 Rubin, K. H. R., Prochaska, J. X., Ménard, B., Murray, N., and David C Koo, D. K., & Phillips, A. C. 2011, *ApJ*, 728, 55
 Rupke, D. S., Veilleux, S., & Sanders, D. B. 2005, *ApJ*, 632, 751
 Rupke, D. S. N., & Veilleux, S. 2011, *ApJ*, 729, L27

- Sato, T., Martin, C. L., Noeske, K. G., Koo, D. C., & Lotz, J. M. 2009, *ApJ*, 696, 214
- Savage, B. D., & Sembach, K. R. 1996, *ARA&A*, 34, 279
- Shapley, A. E., Steidel, C. C., Pettini, M., & Adelberger, K. L. 2003, *ApJ*, 588, 65
- Shen, S., Madau, P., Aguirre, A., Guedes, J., Mayer, L., & Wadsley, J. 2012, *ApJ*, 760, 50
- Shull, J. M., & van Steenberg, M. 1982, *ApJS*, 48, 95
- Simard, L., et al. 1999, *ApJ*, 519, 563
- Sobolev, V. V., & Gaposchkin, S. 1960, *JRASC*, 54, 254
- Socrates, A., Davis, S. W., & Ramirez-Ruiz, E. 2008, *ApJ*, 687, 202
- Steidel, C. C., Bogosavljević, M., Shapley, A. E., Kollmeier, J. A., Reddy, N. A., Erb, D. K., & Pettini, M. 2011, *ApJ*, 736, 160
- Steidel, C. C., Erb, D. K., Shapley, A. E., Pettini, M., Reddy, N., Bogosavljević, M., Rudie, G. C., & Rakic, O. 2010, *ApJ*, 717, 289
- Stocke, J. T., Keeney, B. A., Danforth, C. W., Shull, J. M., Froning, C. S., Green, J. C., Penton, S. V., & Savage, B. D. 2013, *ApJ*, 763, 148
- Strickland, D. K., & Heckman, T. M. 2009, *ApJ*, 697, 2030
- Tremonti, C. A., Moustakas, J., & Diamond-Stanic, A. M. 2007, *ApJ*, 663, L77
- Tripp, T. M., et al. 2011, *Science*, 334, 952
- van de Voort, F., Schaye, J., Booth, C. M., Haas, M. R., & Dalla Vecchia, C. 2011, *MNRAS*, 414, 2458
- Verhamme, A., Schaerer, D., Atek, H., & Tapken, C. 2008, *A&A*, 491, 89
- Verner, D. A., Ferland, G. J., Korista, K. T., & Yakovlev, D. G. 1996, *ApJ*, 465, 487
- Weiner, B. J., et al. 2009, *ApJ*, 692, 187
- Willmer, C. N. A., et al. 2006, *ApJ*, 647, 853
- Zahid, H. J., Kewley, L. J., & Bresolin, F. 2011, *ApJ*, 730, 137